Aerodynamically driven wall-bounded drop motion and rivulet formation

Vom Fachbereich Maschinenbau
an der Technischen Universität Darmstadt
zur
Erlangung des Grades eines Doktor-Ingenieurs (Dr.-Ing.)
genehmigte

Dissertation

vorgelegt von

Dipl.-Ing. Patrick Martin Reinhard Seiler

aus Waiblingen

Berichterstatter:	Prof. Dr.-Ing. Cameron Tropea
1. Mitberichterstatter:	Prof. Dr. Hans-Jürgen Butt
2. Mitberichterstatter:	Apl. Prof. Dr. Ilia Roisman
Tag der Einreichung:	16. April 2019
Tag der mündlichen Prüfung:	3. Juli 2019

Darmstadt 2019

D 17

Seiler, Patrick Martin Reinhard:
Aerodynamically driven wall-bounded drop motion and rivulet formation
Darmstadt, Technische Universität Darmstadt
Jahr der Veröffentlichung der Dissertation auf TUprints: 2019
Tag der mündlichen Prüfung: 3. Juli 2019

Bitte zitieren Sie dieses Dokument als:
URN: urn:nbn:de:tuda-tuprints-82684
URL: http://tuprints.ulb.tu-darmstadt.de/id/eprint/8268

Dieses Dokument wird bereitgestellt von TU Prints, E-Publishing-Service der Technischen Universitaet Darmstadt http://tuprints.ulb.tu-darmstadt.de
tuprints@ulb.tu-darmstadt.de

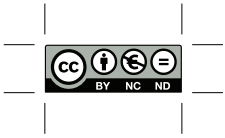

To my mother Helga,
my father Jürgen,
and my grandparents.

Erklärung

Hiermit erkläre ich, dass ich die vorliegende Arbeit, abgesehen von den in ihr ausdrücklich genannten Hilfen, selbständig verfasst habe.

Darmstadt, den 11. Juli 2019

Abstract

Aerodynamically driven wall-bounded drop motion and rivulet formation are two specific cases of gas-liquid flows involving surfaces. These multiphase flows are relevant in many fields, e.g. process engineering, printing, ice accretion, car soiling and exterior water management on vehicles. As the basic physics of these flow phenomena are not entirely understood, further experimental and numerical research is desirable. The present study approaches the topic using generic experiments performed in a wind tunnel. The wind tunnel provides a fully turbulent, two-dimensional channel flow with optical access throughout the test section.

In the first set of experiments single water drops with varying volumes on four different substrates are exposed to the flow in the test section. For a constant gas flow velocity a constant drop motion is observed. The motion is mainly governed by the pressure (drag) induced by the gas flow, by surface tension and the capillary forces associated with the substrate contact angle hysteresis. An appropriate scaling has been found to describe the dimensionless drop velocity (capillary number) in terms of a dimensionless flow *attack* velocity, taking into account the surface wetting properties. The model allows for the prediction of capillary numbers from the attack velocity and it agrees very well with the experimental observations.

A detailed analysis of slow, constantly in a stick-slip manner, moving drops is used to investigate the critical contact angle for moving contact lines.

The second set of experiments investigates the interaction between drops and grooves of variable width. A model predicting whether a drop is absorbed by the groove or passes over the groove is presented.

The final experiments investigate rivulet formation. Through bore holes in the previously used substrates a constant liquid volume flow is injected. For each substrate different behavioral regimes of the resulting rivulets are mapped and described.

Kurzfassung

Durch aerodynamische Kräfte angetriebene, wandgebundene Tropfenbewegung und Rinnsalbildung sind zwei spezifische Arten von Gas-Flüssigkeitsströmungen, bei denen feste Oberflächen involviert sind. Sie spielen in vielen Bereichen eine Rolle, z.B. in der Verfahrenstechnik, im Druckwesen, der Vereisung, der Verschmutzung oder dem Wassermanagement von Fahrzeugoberflächen. Da die zugrundeliegende Physik dieser Strömungen nicht vollständig verstanden ist, bedarf es weiterer experimenteller und numerischer Forschung. Die vorliegende Studie nähert sich dieser Thematik unter Zuhilfenahme eines Windkanals mit einer vollausgeprägten, turbulenten Kanalströmung, dessen Messtrecke optisch zugänglich ist, an.

Zuerst werden einzelne Wassertropfen mit verschiedenen Volumina auf vier verschiedenen Oberflächen untersucht. Bei einer konstanten Gasströmungs- und Tropfengeschwindigkeit unterliegt die Bewegung hauptsächlich dem Strömungswiederstand des Tropfens, der Oberflächenspannung und den Kapillarkräften an der Oberfläche, welche in Form der Kontaktwinkelhysterese in Erscheinung treten. Für dieses System wird mit der dimensionslosen Angriffsgeschwindigkeit und der Kapillarzahl eine geeignete Normierung eingeführt. Aufbauend auf diesen beiden Größen wird ein Modell eingeführt, mit dem sich die Tropfengeschwindigkeit vorhersagen lässt. Eine weiterführende Untersuchung von intermittierend haftenden Tropfen betrachtet den kritischen Kontaktwinkel, bei denen die Kontaktlinienbewegung einsetzt.

Aufbauend auf der Geschwindigkeitsmodellierung wird die Interaktion zwischen Tropfen und einem Einzelspalt variabler Weite untersucht. Passende Normierungen und Nomogramme für die Absorption oder das Überspringen des Spaltes werden vorgestellt.

Abschließend wird die Rinnsalbildung auf verschiedenen Oberflächen und Gas- sowie Flüssigkeitsvolumenströmen untersucht. Die Verhaltensmuster der Rinnsale werden dargelegt, in Regimekarten zusammengetragen und verglichen.

Acknowledgments

First I would like to express my deepest gratitude to Professor Cameron Tropea and apl. Professor Ilia V. Roisman for providing the opportunity to work on my research project at the Institute for Fluid Mechanics and Aerodynamics (SLA) of the Technische Universität Darmstadt. Their ongoing support throughout the last years has made this work possible, providing me with many ideas and offering insights that have helped improve my work.

Second, I am glad to have met Daniel Rettenmaier through our joint research and to be able to now count him among my friends. He has approached aerodynamically driven drop and rivulet motion from a numerical point of view. The hours spent understanding the physics involved in our research are some of the fondest memories I have made during my time in Darmstadt.

I am grateful for the financial support offered by the Adam Opel AG. Their support has enabled me to design, assemble and operate the experimental facilities required for my research. During the last three years I have had many opportunities to meet colleagues from the Adam Opel AG. They have offered great insight on the application side of my research, have suggested improvements and have supplied many of the investigated substrate samples. I want to extend special thanks to Frank Werner and Dr. Philip Klaus, who have both invested a great deal of time during numerous and highly productive meetings.

The framework provided by the Graduate School of Computational Engineering and the Collaborative Research Center 1194 helped me find my bearings at Technische Universität Darmstadt. I am proud to have been an associated member of both groups. Without these memberships none of the interdisciplinary collaborations I was part of would have been possible. Here I want to specifically mention Alexander Saal, Dr. Rüdiger Berger and Professor Hans-Jürgen Butt from the Max-Plank Institute for Polymer Reserach in Mainz as well as Alexander Matei and Professor Stefan Ulbrich from the Department of Mathematics of the Technische Universität Darmstadt.

Without the support of students my research would not have been successful. Many thanks go to Niklas Apell, Vinicius de Campos, Matthias Gerhardt, Mark Gloerfeld, Max Thomas Hasenzahl, Florian Held, Clemens

Janzarik, Simon Matthes, Andreas Mayrhofer, Jannis Reusch, Robin Robrecht, Matthias Schäfer, and Robin Wickersheim.

Additionally, I want to thank all current and former colleagues for a great time at the campus in Griesheim. A lot of discussions, especially with Maximilian Kuhnhenn, Jan Breitenbach, Johannes Feldmann, Fabian Tenzer, and Andreas Bauer have enhanced the outcome of this thesis.

Many special thanks go to Erin Koos, Daniel Rettenmaier, Tobias Ecker and Christian Seiler for proof-reading parts of this thesis.

Last but not least I want to thank my family and friends for their support during my time in Darmstadt as well as throughout all of the steps that lead me here. Without the support of my parents, Helga and Jürgen as well as my brother, Christian, my studies would not have been possible. I am grateful for the support Susanne Döring offered. I especially wanted to mention Tobias Ecker, who always has been encouraging me in my endeavors, Daniel Kallfaß, who kept me grounded and Flora Siebler with her unwavering support.

Thank you.

Patrick

Contents

1 Introduction

Over the last decades, great efforts were made to understand dynamically interacting *gas-liquid flows*. These involve combinations of both miscible and immiscible fluids. In the latter case they form a phase boundary between them. The interface between water and air is the most commonly known example for such a boundary. If additionally a solid substrate is involved which interacts with both fluids, a three-phase system needs to be considered. Examples for such systems are the drying of wet surfaces, fuel mixing processes in jet engines and the tears of wine patterns in whisky tumblers, scientifically know as the Marangoni effect. One aspect of such systems is the *three-phase contact line*. It is the intersection between both fluid phases and a solid. If a contact line moves the involved substrate is either wetted or dewetted. Both occurs in close spatial proximity when drops and rivulets move over a surface. Even though, contact lines as well as *wetting* and *dewetting* of substrates have been subject of many studies they and specifically the motion of aerodynamically driven drops and rivulets, up to date have not been fully understood yet.

The extensive research in this field is strongly related to many industrial applications benefiting from a deeper understanding of these dynamic, multiphase systems. Among them are printing, spray coating (Dimitrakopoulos and Higdon, 1997; Cristini and Tan, 2004), spray cooling, oil recovery (Madani and Amirfazli, 2014; Schleizer and Bonnecaze, 1999; Mahé et al., 1988; Bear, 1972), lubrication processes as well as system involving condensation.

Two-phase flows are not limited to industrial applications but also play a role in many environmental processes. It concerns aviation in-flight icing (Tarquini et al., 2014; Theodorsen and Clay, 1933) as well as automotive water management (Hagemeier et al., 2011). For applications where a surface moves through a gaseous phase (e.g. vehicles or planes), drop or rivulet motion by aerodynamic forces is predominant. The interaction of the liquid

with the ambient flow are equally important as the wetting characteristics of the fluid on the surface.

1.1 Motivation

The work presented in this study has been motivated by the desire to predict *wall-bounded drop motion* as well as *rivulet formation*. Their importance is highlighted using an example from automotive exterior water management (EWM). One aspect of EWM is the flow of water over the surface of a car while driving, which is wall-bounded liquid motion.

Car manufacturers are required to provide experimental results, showing how water behaves on the car surface, in order for an new vehicle design to be certified for road use. Binding for all countries of the European Union is the European legal directive Nr. 661/2009 (2009). These strict requirements result from the increased probability of an accident while driving in rainy conditions. Statistical data (Destatis, 2017) compiled by the German Federal Statistical Office show that accidents are twice as likely on rainy days. The statistical data does not distinguish between accident causes. However, the poor conditions of the road, i.e. increased braking distance or aquaplaning, as well as the driver's inhibited traffic overview due to water, are most certainly likely reasons for this increase. The driver's visibility may additionally be compromised by drops contaminated with particles, primarily originating from a preceding vehicle (Paulsen, 2017). Considering the regulations and resources invested by the manufacturers concerning water management, the latter cause is deemed to be non-negligible.

An image of such a wind tunnel experiment is shown in Figure 1.1. It was taken in an environmental wind tunnel during an experiment that simulated driving at 100 $^{\mathrm{km}}/_{\mathrm{h}}$ in dense rain. A fluorescent dye, which is excited by ultraviolet light and emits in the visible spectrum, was added to the water. By filtering the ultraviolet wavelengths and only passing light in the visible spectrum at the camera, the wetting pattern on the vehicle surface is visualized.

In some areas of the vehicle, an active system is used to dewet the substrate: the windshield wiper is a good example. Such an active system is not viable for every vehicle surface which has to be kept clear. The side

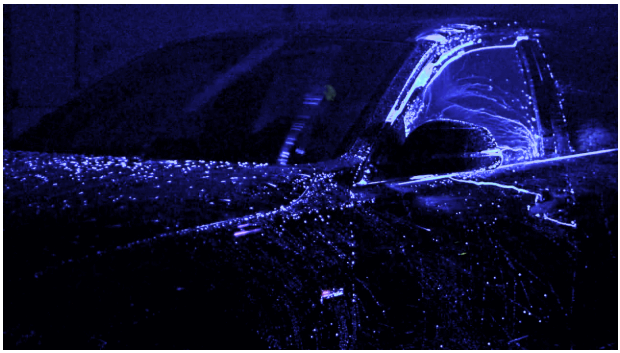

Figure 1.1: Visualization experiment of wetting patterns on a full-scale car in an environmental wind tunnel.

window and wing mirrors are two examples for components that need to be designed to avoid liquid accumulating in viewing areas. Besides keeping the driver's line of sight clear, ensuring the functionality of sensors is paramount. In recent years the number of sensors assisting the driver or used for autonomous driving has steadily increased. Faulty measurements due to liquid accumulation could therefore severely compromise passenger safety.

While developing a new car model, vehicle manufacturers have used full-scale experiments with prototypes in environmental wind tunnels to determine how the rain or splashed road water interacts with the vehicle. Analytically or numerically predicting the liquid behavior on the car surface is currently only possible within strict constraints. However, aerodynamically driven wall-bound multiphase flows are not yet entirely understood; only few models are available in published literature. Second, the problem spans a wide range of length scales, from meters - the length of the vehicle - to nanometers at the contact line. As a result, the numerical simulations are always a trade-off between accuracy and computational cost.

The aim of this work was to expand the understanding of wall-bounded multiphase flows by two means. First, by providing new, physics based models that allow prediction of the behavior of aerodynamically driven wall-bounded drops. Second, strengthening the foundation of experimental data that can be used to validate numerical simulations.

1.2 Objectives and outline of this work

For achieving the above stated goals, generic and reproducible experiments are well suited. Although there are many aspects to wall-bounded fluid flow, the present study focuses primarily on two: the constant motion of single drops and the formation of rivulets in a turbulent gas flow. In this way the investigations complement parallel running investigations at the Technische Universität Darmstadt addressing other issues of wall-bounded fluid flow, e.g. (Rettenmaier, 2019). For the investigations of this study a wind tunnel with a well defined and reproducible turbulent flow was required. Such a tunnel was designed, manufactured and commissioned as part of this study. It offers the possibility to investigate the behavior of individual drops as well as injecting a constant flow of liquid onto different substrates, thus producing an aerodynamically driven rivulet. The behavior of the liquid on different substrates can be observed through transparent walls and ceiling.

Chapter 2 briefly summarizes the theoretical foundation that this work is based on.

Chapter 3 describes the wind tunnel and experimental techniques used in the investigations.

A study on aerodynamically driven, wall-bounded single drop motion is presented in **Chapter 4**. From the observations a physics based model connecting the flow parameters to the drop velocity is provided.

Chapter 5 builds on the model and scaling of single drop motion by investigating how drops behave when encountering a sharp edged groove. The relevant forces acting on a drop when it encounters a single groove are highlighted and monograms delimiting each outcome are shown.

Chapter 6 deals with the formation of rivulets due to aerodynamic forces. The conditions required in order for a rivulet to form is investigated on various substrates.

Chapter 7 concludes this work and presents an outlook for further investigations.

In **Appendix A** a long-term study of surface contact angles on a car, exposed to environmental influences, is presented. This research was conducted for three reasons. First, contact angles play a central role for all models and observations of this work. Second, exterior water management

was one of the motivations behind this research. Lastly, few publications on real world influences on surface properties are published.

2 Background and Theoretical Considerations

This chapter provides an overview of the literature relevant for this work. Fundamental physical principles concerning wetting are introduced.

Parts of this chapter have been published in Seiler et al. (2019).

2.1 Dimensionless parameters influencing the phenomena

This section introduces the relevant dimensionless parameters used in this work.

Capillary number

When considering fluid motion it is often beneficial to introduce a dimensionless parameter characterizing the velocity of the contact line u. For a moving liquid phase the capillary number

$$\mathrm{Ca} = \frac{u\mu}{\sigma} \tag{2.1}$$

is such a dimensionless description. The characteristic velocity u is made dimensionless with the dynamic viscosity μ and the surface tension σ (liquid/gas). The Capillary number expresses the ratio of viscous to surface tension forces.

Reynolds number

The Reynolds number relates the inertial forces to the viscous forces of a flow. It is defined as

$$\mathrm{Re} = \frac{\varrho u L}{\mu}\,, \tag{2.2}$$

where ϱ is the density of the fluid, u the velocity of the flow, L a characteristic length and μ the dynamic viscosity.

Weber number

The Weber number compares inertial to surface forces,

$$\mathrm{We} = \frac{\varrho u^2 L}{\sigma}\,. \tag{2.3}$$

Analogous to the Reynolds number ϱ is the density of the fluid, u the velocity of the flow and L a characteristic length. The surface tension is represented by σ.

Bond number

The ratio between volume forces (e.g. gravity, magnetic, electrical) and surface forces of liquids is expressed in the Bond number

$$\mathrm{Bo} = \frac{\mathcal{F} L^2}{\sigma}. \tag{2.4}$$

The force density per unit volume is represented by $\mathcal{F}$, the characteristic length by L and the surface tension by σ.

2.2 Static contact angle

A contact line forms at the intersection of a fluid-fluid phase boundary and solid substrate. The resulting angles and shape of the phase boundary depend on the properties of the three phases. Contact angles as well as contact line related phenomena are introduced in this section, in particular for the case of a gas-liquid-solid, three-phase contact line.

2.2.1 Equilibrium contact angle

The shape a liquid forms at the three-phase contact line depends on the acting forces. A sketch of a three-phase contact line is shown in Figure 2.1. The vectors represent the forces acting on the three phase interfaces and are commonly expressed as the respective surface tensions (force/length), $\sigma_{\mathrm{liquid-solid}}$, $\sigma_{\mathrm{liquid-gas}}$ and $\sigma_{\mathrm{solid-gas}}$.

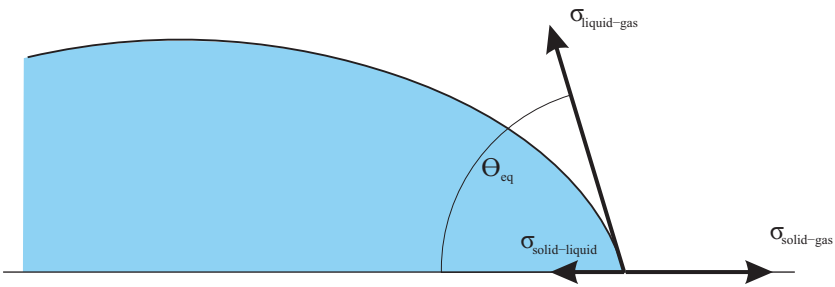

Figure 2.1: Sketch of an equilibrium contact angle of a liquid-gas-solid contact line. Surface forces (surface tension) at each phase interface are represented by vectors.

As seen in Figure 2.1, an angle $\Theta_{\text{eq.}}$ is introduced between $\sigma_{\text{liquid}-\text{solid}}$ and $\sigma_{\text{liquid}-\text{gas}}$. This angle is the equilibrium contact angle. The equilibrium contact angle can be calculated by invoking a balance of the horizontal forces acting, yielding the Young equation (Young et al. (1805)):

$$\sigma_{\text{solid}-\text{gas}} = \sigma_{\text{liquid}-\text{solid}} + \sigma_{\text{liquid}-\text{gas}} \cos \Theta_{\text{eq}} \tag{2.5}$$

The example shown in Figure 2.1 is referred to as a partially wetted state, whereby there are two limits for Θ_{eq}: First, complete wetting of the substrate, where $\Theta_{\text{eq}} = 0$. In Eq. 2.5, this implies $\sigma_{\text{solid}-\text{gas}} = \sigma_{\text{liquid}-\text{solid}} + \sigma_{\text{liquid}-\text{gas}}$. Second, non-wetting of the substrate, where $\Theta_{\text{eq}} = 180°$. In this non-wetting state, a gaseous layer is present between the substrate and the fluid and there is no contact between them. No three phase contact line forms (Bonn et al. (2009)). The contact angle is therefore a measure of the wettability of the fluid/gas/substrate combination. Contact angle measurements, however, are influenced by other factors.

2.2.2 Apparent contact angle

For the definition of the equilibrium contact angle in section 2.2.1, an ideal smooth and chemically homogeneous substrate was assumed. Engineering surfaces are neither ideally smooth nor chemically homogeneous. For this reason both imperfections need to be considered in greater detail. Chemical heterogeneity are clusters of different molecules at the substrate surface.

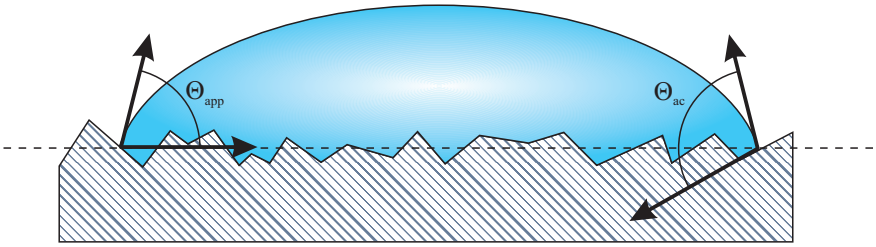

Figure 2.2: Sketch of a contact line on a rough, chemically homogeneous surface showing the difference between apparent and actual contact angle. (Adaption from Tropea et al. (2007))

Because the contact angle is dependent on the combination of surface properties of the involved phases, it is clear that locally different contact angles can appear on the same surface. As for the roughness, a closer look at the area near the contact line is necessary. In Figure 2.2, the sketch of a contact line on a rough, chemically homogeneous surface is shown. The dashed line represents the surface as can be perceived macroscopically. The solid line represents the actual surface with local roughness. From the macroscopic viewpoint, the measurable contact angle corresponds to $\Theta_{\mathrm{app}} = 90°$. On a microscopic scale the actual contact angle is $\Theta_{\mathrm{ac}} \approx 130°$, which corresponds to the angle one would obtain using the Young equation, Eq. (2.5). With current technological methods, it is not possible to measure the actual contact angle (Tropea et al. (2007)) and the measurable apparent contact angle depends to great extent on the local surface roughness.

2.3 Dynamic contact angle

On real, non-ideal surfaces, multiple equilibrium states exist. Two identical sessile drops can exhibit different equilibrium contact angles on the same surface, depending on the local surface roughness, inhomogeneities, as well as the time history of the drop, i.e. the previous state of the drop. There are two limits to the equilibrium state for most engineering surfaces. These limits are called the critical advancing contact angle $\Theta_{\mathrm{adv.,cr}}$ and critical receding contact angle $\Theta_{\mathrm{rec.,cr}}$. If $\Theta_{\mathrm{adv.}} > \Theta_{\mathrm{adv.,cr}}$, the three-phase contact

line moves, wetting new substrate regions. De-wetting of the substrate occurs when $\Theta_{\text{rec.}} < \Theta_{\text{rec.,cr}}$.

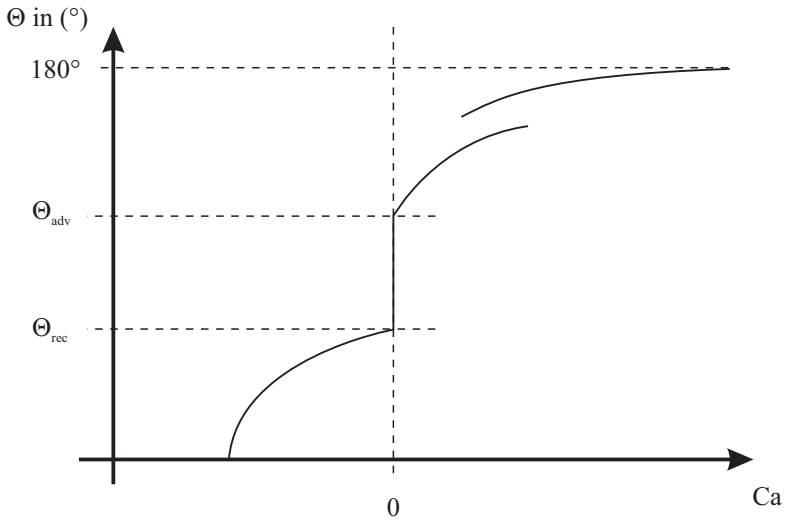

Figure 2.3: Diagram qualitatively showing the relationship between contact line velocity and apparent contact angle (adaptation from Blake (2006)).

Between contact line velocity and apparent contact angle, a semi-empirical relation exists, as shown in Figure 2.3. It shows the contact line velocity, expressed by the capillary number (see section 2.1) on the abscissa and the apparent contact angle on the ordinate. For this diagram, negative velocities represent de-wetting processes and positive velocities wetting processes.

At $\text{Ca} = 0$, the hysteresis with both critical angles can be seen. For $\text{Ca} < 0$, the contact angle tends toward zero. If the driving force of the de-wetting process is sufficiently strong, such that the angle becomes zero, a residual film remains while the majority of the volume moves along the surface. On the wetting side $\text{Ca} > 0$ a bi-modal jump is present (Blake, 2006). For the same contact line velocity two contact angles can occur. The contact line history determines the case. In the present study the contact line velocity is at least one order of magnitude smaller than this bi-model state.

2.3.1 Hydrodynamic theory

Hydrodynamic theory is one possible approach to describe dynamic wetting and de-wetting. It is based on continuum mechanics. The issue with continuum mechanics and a moving wetting line is the no-slip assumption at boundaries. A moving wetting line contradicts this condition. Following the interpretation of Blake (2006), a movement at the wall would require an infinite force acting from the fluid on the surface. In reality, this is not the case. Relaxing the no-slip condition near the wall as Kistler (1993) suggested, is one solution for this contradiction.

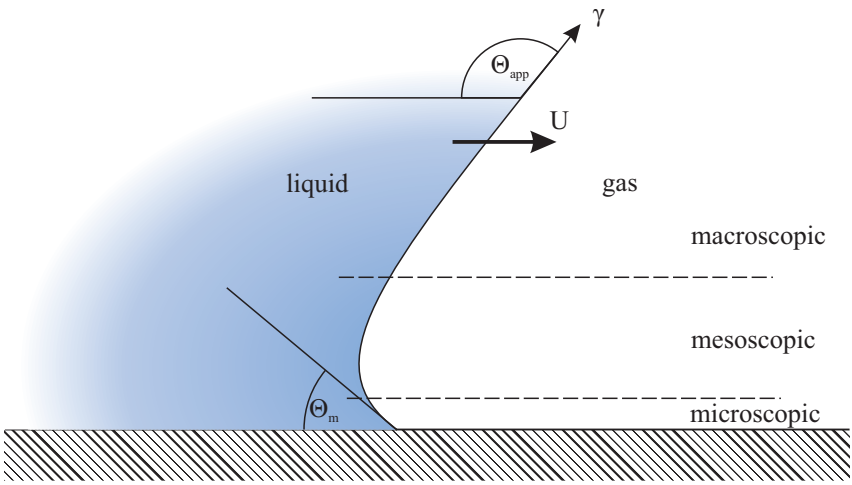

Figure 2.4: Sketch showing the relation between the actual contact angle on a microscopic scale and the observable dynamic contact angle (adapted from Blake (2006))

Besides relaxing the no-slip condition, another simple solution is to not specifically consider the region near the three-phase contact line. Figure 2.4 shows a sketch of the three-phase contact line, highlighting three distinct length scales. The meniscus formed near the substrate can be clearly seen as well as the distinction between actual and apparent contact angle. By

assuming $\Theta_{\text{microscopic}} = \Theta_{\text{ac, eq.}}$, $\Theta_{\text{D}} < 135°$ and small capillary numbers, a continuum mechanics description of wetting is possible.

$$\Theta_{\text{D}}^3 - \Theta_{\text{m}}^3 = 9\text{Ca } \ln\left(\frac{L}{L_{\text{m}}}\right) \tag{2.6}$$

where L corresponds in this case to the chosen macroscopic length scale and L_{m} to the microscopic length scale. Typically, $\ln(L/L_m) = 10$ for completely wetting fluid - surface combinations, a case which is not present in this study. When conducting experiments, a scatter of the L and L_m values is to be expected. (Voinov (1976))

Subsequently Voinov (1976) generalized Eq. (2.6) for dynamic contact angles $\Theta_{\text{D}} > 135°$. In addition, he highlights that the assumption $\Theta_{\text{microscopic}} = \Theta_{\text{ac, eq.}}$ is generally not applicable. Voinov (1976) indicates that the microscopic contact angle is velocity dependent.

2.3.2 Molecular-kinetic theory

Molecular-kinetic theory offers an alternative approach to model wetting processes. As the name suggests, the motion of the three-phase contact line is described by molecular motion. The motion of molecules cannot be described by continuum mechanic equations. Instead, random statistical displacements of the molecules in the three-phase area are considered. Cherry and Holmes (1969), Blake and Haynes (1969), and Ruckenstein and Dunn (1977) were the first researchers to formulate this idea.

Figure 2.5 shows a sketch of the three-phase contact area according to molecular kinetic theory. The random displacement of a molecule near the surface corresponds to the diffuse boundary of a liquid-gas interface. In an equilibrium state, molecules oscillate between points of adhesion near the contact line. The characteristic frequency of these oscillation is described by (Blake (1993)):

$$\kappa_{\text{eq}} = \frac{k_{\text{B}}}{h} \exp\left(\frac{-\Delta G_w^* t}{N_{\text{A}} k_B T}\right). \tag{2.7}$$

Equation 2.7 consists of the Boltzmann constant k_{B}, Planck constant h, Avogadro number N_{A}, absolute temperature T and $\Delta G_w^* t$ the activation

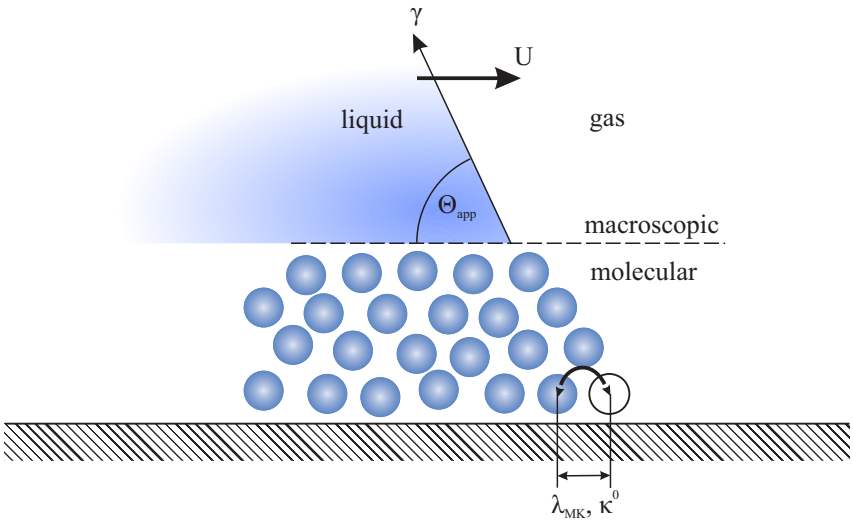

Figure 2.5: Sketch of the molecule displacement process in molecular kinetic theory (adaption form Blake (2006))

free energy of wetting. A local increase in frequency due to an external force results in substrate wetting. Analogously, a decrease in frequency results in de-wetting. In order to move the contact line, a net frequency corresponding to molecule motion can be determined. This frequency can be calculated using w_{MK} (work per unit displacement) and the unit length on the wetting line. Using the displacement frequency and the distance between adsorption sites λ_{MK}, as shown in Figure 2.5, the work w_{MK} corresponding to the wetting line velocity U is found:

$$U = \kappa_{\mathrm{net}}\lambda_{\mathrm{MK}} = 2\kappa_{\mathrm{eq}}\lambda_{\mathrm{MK}} \sinh\left(\frac{w_{\mathrm{MK}}}{2nk_BT}\right), \tag{2.8}$$

where n is the number of adsorption sites per unit area. A detailed description of all relevant equations can be found in Blake (1993) and his later publication Blake (2006). He shows that a connection between the wetting velocity U and the dynamic contact angle Θ_D can be established via the force required to move the contact line. The force per unit length on the wetting line is

$$F_w = \sigma(\cos\Theta_{\mathrm{eq}} - \cos\Theta_{\mathrm{D}}). \tag{2.9}$$

Combining equation 2.8 and 2.9 results in

$$U = 2\kappa_{\mathrm{eq}}\lambda_{\mathrm{MK}} \sinh\left(\frac{\sigma\lambda_{\mathrm{MK}}^2(\cos\Theta_{\mathrm{eq}} - \cos\Theta_D)}{2k_BT}\right). \tag{2.10}$$

Blake (2006) cautions about the uncertainties remaining in this equation. For example, κ_{eq} is subject to variation and later publications (Blake and De Coninck, 2002) imply that the velocity also depends on the fluid viscosity.

2.3.3 Further wetting models

The models introduced in section 2.3.1 and 2.3.2 are limited to $\Theta < 180°$ and Ca numbers of an order of magnitude $\mathcal{O}(\mathrm{Ca}) = 0.1$. The need to exceed the limitation in capillary number resulted in the development of further models. A combined model of hydrodynamic and molecular kinetic theory improved the correlation between theory and experimental results, but is still limited to $\mathcal{O}(\mathrm{Ca}) = 0.1$, (Blake, 2006).

Shikhmurzaev (1993) suggested a fundamentally different approach to wetting. His model accounts for the dissipation within the formation process of the liquid solid interface, as summarized by Lauga et al. (2007). It assumes that molecules flow from the gas-liquid surface to the liquid-solid interface. The parameter change during this transition at the interface needs a finite time. During this adaption time, large gradients, e.g. in surface tension, that effect the fluid motion near the contact line occur. Calculating the analytical solution for the model introduced by Shikhmurzaev (1993) yields remarkable agreement with experimental results, as shown by (Blake, 2006). The model resolves the conflict of the singularity in the vicinity of the wetting line. However, it relies on coefficients that vary with flow conditions and are difficult to predict (Blake, 2006).

2.3.4 Critical dewetting capillary number

The velocity of a dewetting contact line is limited. This critical velocity is expressed in the dimensionless capillary number $\mathrm{Ca}^\star$. Cases for which the absolute value of the receding capillary number is larger than $\mathrm{Ca}^\star$ the contact line propagation becomes unstable, eventually leading to its breakup, were observed. This phenomenon was discussed in (Shing Chan et al., 2011; Maleki et al., 2007; Sedev and Petrov, 1991; Snoeijer et al., 2007).

One empirical correlation that can be used to determine $\mathrm{Ca}^\star$ is based on the experiments of Kistler (1993)

$$\Theta_D = f[\mathrm{Ca} + f^{-1}(\Theta)], \tag{2.11}$$

where Θ is the static contact angle (static advancing or static receding), $f^{-1}(\cdot)$ is the inverse function of the Hoffman function $f(\cdot)$ defined as

$$f(x) = \arccos\left\{1 - 2\tanh\left[5.16\left(\frac{x}{1+1.31x}\right)^{0.71}\right]\right\}.$$

This model predicts that at some critical value $\mathrm{Ca}^\star$, based on the magnitude of the dewetting velocity, the receding dynamic contact angle converges to zero. Condition $\Theta_D = 0$ in Eq. (2.11) yields

$$\mathrm{Ca}^\star = 0.23\left(\operatorname{arctanh}\left[\frac{1-\cos\Theta_{\mathrm{rec}}}{2}\right]\right)^{1.41}. \tag{2.12}$$

3 Experimental Facility

In this chapter the experimental facility used throughout this study is introduced. It consists of three major parts. The core of the experiment is the wind tunnel in which the flow is controlled by a fully automated system. It allows setting and recording all relevant flow parameters. In addition the control system allows triggering and synchronizing the image acquisition hardware. For image acquisition different high-speed cameras and LEDs are used.

Parts of this chapter have been published in Seiler et al. (2019).

3.1 Wind tunnel and test section

The wind tunnel used for this study is designed to obtain a fully developed, turbulent channel flow in the test section. The basic concepts concerning channel flows were introduced by Reynolds (1883). In a fully developed channel flow the velocity gradient is zero in streamwise direction.

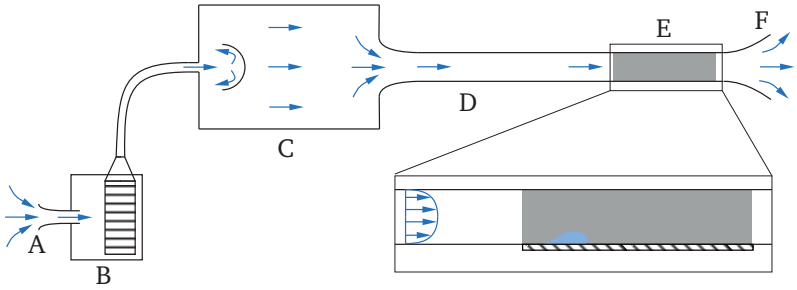

Figure 3.1: Schematic of wind tunnel with following components: A - inflow nozzle, B - radial blower, C - settling chamber with flow inverter, D - acceleration nozzle and channel, E - test section and F - exit diffuser

Figure 3.1 shows a schematic of the wind tunnel used for the experiments. The components of the facility are marked in order of the gas flow.

Filtered ambient air is sucked in through in inflow nozzle (A) which is used to measure the volume flow rate of the channel. This nozzle is directly attached to the suction side of an Elektror HDA-FUK 0,75 radial blower (B). The rotational speed of the engine driving the fan is controlled by a frequency converter it is set via the data acquisition and control (DAC) unit.

From the blower outlet a flexible tube directs the flow into a settling chamber (C). The flexible connection decouples the blower from the settling chamber and test section therefore avoiding vibrations in the test section. Behind the inlet of the chamber a flow baffle is mounted decelerating the flow. The chamber has a diameter of 0.8 m and length of 1 m. Temperature and overpressure in the chamber are monitored. The temperature of the settling chamber is measured using a thermocouple of type T and the pressure difference between chamber an environment by a Setra 264 pressure transducer. The transducer has a full scale accuracy of $\pm 0.4\%$.

Figure 3.2: Photograph of the wind tunnel facility.

The gas flow is accelerated through a nozzle with a contraction ratio of 9:1 in height and 3:1 in width. The subsequent channel consists of two parts: a transition area (D) and a test section (E). Both are of equal cross section with a height of $\mathcal{H} = 15$ mm and width of $\mathcal{W} = 200$ mm. The aspect ratio

$AS = 13.3$ is constant in the streamwise direction. The transition area (D) with a length $\mathcal{L} = 80\ \mathcal{H} = 80 \cdot 15 \times 10^{-5}$ m $= 1.2$ m is required for the flow to fully develop. The flow field being fully developed after the transition area it flows seamlessly into the test section (E). At the end of the test section (E) an exit diffuser (F) is attached. Same as the nozzle it is 3D-printed and reduces the pressure loss at the end of the tunnel. Dealing with a sub-sonic flow the flow is decelerated by an increase in cross section area by 2.5. In order to prevent flow separation from the diffuser walls no angle is greater than 10°.

A photograph of the wind tunnel used for the experiments is shown in Figure 3.2. The image shows the settling chamber (C) on the left hand side. The imaging hardware described in Section 3.3 was removed allowing an undisturbed view on the channel.

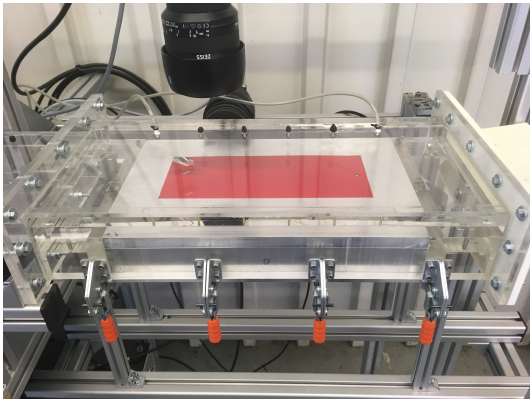

Figure 3.3: View of the test section.

The test section (E) as well as a part of the exit diffuser (F) are depicted in Figure 3.3. The test section forms the central component of the wind tunnel. Three sides: top and both sides are made from acrylic glass enabling optical access. The floor of the channel is manufactured from aluminum and is removable. The aluminum frame allows to mount different substrates samples. A steel sample, which was varnished in the Adam Opel AG (Rüsselsheim) assembly line, is shown mounted in the test section of the wind tunnel. The 0.25 m long and 0.1 m wide sample is aligned with the channel floor in order

to form a gapless test section floor. The test section is manufactured with absolute tolerances smaller than 0.1 mm. These high demands in accuracy need to be met in order for a fully developed and undisturbed turbulent channel flow to form within the test section. The floor of the test section is designed in such a way that it can be easily removed. This allows exchanging the mounted samples quickly as well as providing access to the samples throughout a set of experiments. Cleaning the substrate in order to ensure identical experimental conditions is paramount.

On the far side of the test section pressure taps are located in stream wise direction as shown in Figure 3.3. The measure the pressure loss in the tunnel. From the pressure loss the wall shear stress can be calculated. The pressure loss in stream wise direction is measured using a Setra 263 transducer with an accuracy of 0.14% FS.

Two iDS cameras, one used for shadowgraphy imaging and the other for a top view of the drop, are mounted. Further details on the imaging systems used for this study is found in Section 3.3.

3.1.1 Volume flow measurement

Knowing the gas flow velocity in the test section is essential. Measuring the gas volume flow using the inflow nozzle (A) shown in Figure 3.1 is a practical method doing this. In the setup a quarter circle measurement nozzle ("Viertelkreismessdüse") as defined in the norm DIN EN ISO 5801 (2011) is used.

A cross-section sectional view of the inflow nozzle is shown in Figure 3.4. The displayed dimensions are scaled on the $\mathcal{D}_{\text{nozzle}} = 50$ mm diameter. The pressure difference Δp_{nozzle} between the averaged value of the four pressure taps and the ambient pressure p_∞ is measured. Due to the shape of the nozzle the velocity distribution at the pressure taps is uniform.

A Setra 239 differential pressure sensor with a full-scale accuracy of 0.14% measures the differential pressure Δp_{nozzle}. To calculate an accurate volume flow rate the environmental parameters need to be considered. A calibrated type T thermocouple measures the ambient temperature, the relative humidity ϕ is recorded by a Bosch BME sensor with a full scale accuracy of 3% and the ambient pressure p_∞ is provided by a Kobold SEN-3245/2B035 sensor with an accuracy of 0.5% FS.

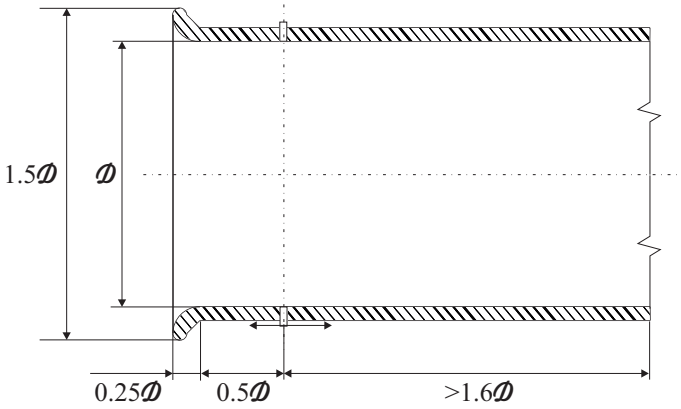

Figure 3.4: Cross section of circular volume flow measurement nozzle. (DIN EN ISO 5801, 2011)

Using the equations provided by DIN EN ISO 5801 (2011) it is possible to calculate the volume flux through the nozzle. Airtight seals between each component of the wind tunnel ensures that there is no leakage and mass loss. Due to this the volume flux in the nozzle must correspond to the volume flux in the test section. Using the incompressible continuity equation and the cross-sectional area of the channel allows calculation of the mean gas flow velocity. The assumption of a incompressible flow is valid because the Mach number Ma is small than 0.1 for the maximal channel velocity.

3.1.2 Flow field validation and verification

The velocity profile for two channel Reynolds numbers in the turbulent regime is shown in Fig. 3.5, measured using a single hot-wire probe. The red solid line represents the lowest investigated $Re_{\mathcal{H}} = 10 \times 10^3$ and the blue dashed line is near the upper limit of the tunnel at $Re_{\mathcal{H}} = 30 \times 10^3$. These profiles are compared to direct numerical simulations (DNS) from Moser et al. (1999), confirming the fully developed state of the flow. For some positions bars representing the estimated deviation of the probe position are shown. These fluctuations arise primarily from minor vibrations of the probe holder, which had to be inserted 500 mm into the channel from the exit plane. An increase of the channel flow velocity to $Re_{\mathcal{H}} = 35 \times 10^3$,

corresponding to a mean flow velocity of $\bar{U} \approx 33$ m/s, exhibits a similar normalized velocity profile; hence, the flow can be assumed to be a fully turbulent, two-dimensional pressure driven channel flow.

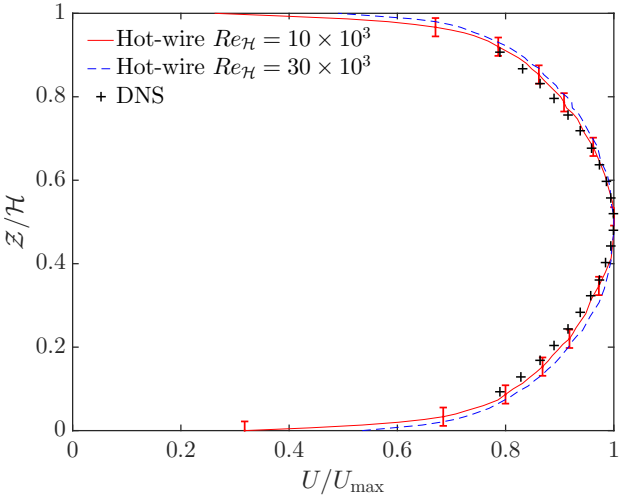

Figure 3.5: Normalized hot-wire measurements of the velocity profile in the test section for $Re_{\mathcal{H}} = 10 \times 10^3$ and $Re_{\mathcal{H}} = 30 \times 10^3$ compared to direct numerical simulations (DNS) from Moser et al. (1999). (Reprinted from Seiler et al. (2019), with permission of © 2019 APS Physical Review Fluids.)

The turbulence intensity as defined in Schlichting and Gersten (2006) is

$$\mathrm{Tu} = U_{\mathcal{H}} \sqrt{\frac{1}{3}\left(\overline{U_{\mathcal{X}}'^2} + \overline{U_{\mathcal{Y}}'^2} + \overline{U_{\mathcal{Z}}'^2}\right)} \tag{3.1}$$

where $U_{\mathcal{H}}$ is the mean channel flow velocity and $\overline{U'^2}$ corresponds to the time averaged flow fluctuations of each velocity component. In Figure 3.6 these turbulence intensities for different channel Reynolds numbers are compared. In the diagrams the $\mathcal{Z}$-coordinate, from floor to ceiling of the wind tunnel, is normalized by the tunnel height $\mathcal{H}$.

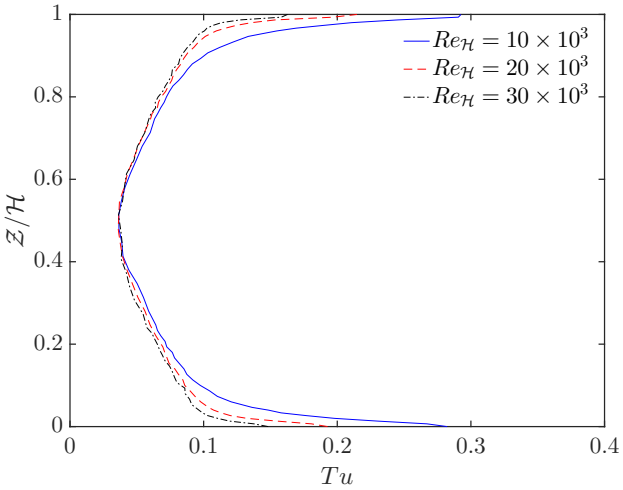

Figure 3.6: Turbulence intensity calculated from hot-wire measurements in the test section for different Reynolds numbers. (Reprinted from Seiler et al. (2019), with permission of © 2019 APS Physical Review Fluids.)

3.2 Control system

The control interface connects the distinct input and output signals to a computer. A National Instruments USB-6351 multifunction I/O-device (DAQ) is used for most task. It is independently powered and is connected to a computer via USB. Since the measurement principle of thermocouples requires a defined input they cannot be connected to the USB-6351 DAQ. A NI Speed USB Carrier USB 9162 using a NI 9219 card is used to measure the environmental and settling chamber temperature.

The signals of both DAQ devices are processed by a virtual instrument (VI) developed specifically for the wind tunnel using NI LabView. The VI was created in order to achieve four tasks.

First, is converts the analogue voltage signals using calibration parameters to their corresponding values. The pressure sensors as well as the radial blower use such signals. The signal provided by the blower indicates the current rotational speed of the fan. After conversion the program performs calculations. From ambient temperature, pressure, humidity as well as the pressure difference at the nozzle the volume flux is calculated. Using the

volume flux and channel geometry the mean gas flow speed in the test section as well as channel Reynolds number $\mathrm{Re}_{\mathcal{H}}$ is determined. All flow parameters are sampled at 2 - 8 kHz, depending on the imaging frequency used during the experiments.

Second, the VI allows controlling the fan. For this two signals are required: a 5V transistor-transistor logic (TTL) enabling signal, closing the relay circuit to the engine and a 0 - 5 V signal which is mapped in the frequency converter to 0 - 100 % rotational speed.

Third, from the VI the imaging devices described in Section 3.3 can be triggered and synchronized. On the one hand the devices are synchronized with each other. On the other hand the images are synchronized with the corresponding flow parameters. Triggering occurs using an accurate clock within the DAQ.

Lastly, the VI offers the possibility to automatically store all experimental data to a technical data management streaming (TDMS) file. The program stores the raw data from each sensor without any calibration, the calibrated values and the calculated values. During post processing the calculated values are double checked ensuring their validity.

One of the most important checks for a measurement system is its step response. It characterizes how fast a system reacts to an abrupt change in signal. The step behavior of the volume flow measurement was determined by comparing the volume flux measurements with hot-wire measurements. Hot-wires sampling at frequencies above 10^4 Hz are ideal for this application. The comparison showed that the delay between change in flow value and signal is smaller than the quickest sampling frequency.

Another important check is ensuring that the mean gas flow velocity calculated from the volume flux corresponds with the actual value. Using the detailed hot-wire measurements as exemplary shown in Figure 3.5 a deviation between both measurement techniques of less than 3 % was found. Considering the limitations in the positioning of the hot wire probe (as describe in Section 3.1.2) this an acceptable discrepancy.

3.3 Imaging

Images of drop and rivulet behavior on substrates are recorded through the transparent walls and ceiling of the test section. The shadowgraphy technique shown in Figure 3.7 has been used for experiments with drops in order to quantify them. This quantification has been done by image analysis, which is explained in Section 3.4.

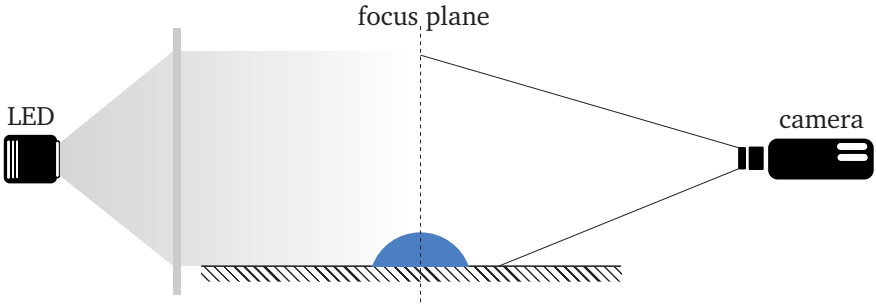

Figure 3.7: Shadowgraphy setup with light source, diffuser plate, object and camera.

All experiments have been conducted using Veritas Constellation 120E28 5600K LED arrays or Veritas Constellation mini 120E28 5600K LED light sources. Both arrays emit 22000 lm and can be triggered by a 5 V transistor-transistor logic (TTL) signal. Both properties make them well suited for high speed imaging.

For this study, two different cameras have been used to record the images. The major part of observations have been made using two iDS UI-3180CP-M-GL Rev. 2 monochrome cameras with Zeiss Milvus 2/50mm macro lenses. These camera records 12 Bit monochrome images with a resolution of 0.4 Mpx at 150 frames per second (fps). The combination between lens, sensor and focus plane resulted in a spatial resolution of 23 $\mu\mathrm{m}/\mathrm{px}$. At $f/5.6$ and a focal distance of 200 mm the depth of field is 1.7 mm. The magnification for this configuration is 1 : 2.4. The shutter speed for all recordings has been set to 6 μs. Diffraction of the lens aperature does not need to be considered, the diameter of the Airy disk at $f/5.6$ is $d_{\mathrm{Airy,\ 680\ nm}} = 4.6\ \mu$m being smaller than the sensor pixel size 4.8 μm (Hecht, 2002). The iDS

cameras have been used to determine the overall behavior of the drops while moving along the substrate.

The second camera used for the observations was a Phantom v12.1 high speed camera. It has a resolution of 1280×800 pixels at 12 Bit and records up to 6242 fps. The pixels have a size of 28 μm, diffraction again does not need to be considered. The recordings have been made using a Nikon Micro-Nikkor 105mm 1:2.8 macro lens at a working distance of 200 mm, leading to a spatial resolution of 23 $^{\mu m}/_{px}$ at a magnification of 1.2:1. In this configuration the depth of field is 1.5 mm. All high speed images for this study have been recorded at 4000 fps with an exposure time of 3 μs.

3.4 Image processing

In order to analyze each recorded shadowgraphy image a dedicated program has been developed. The individual steps taken to extract the information for each image are shown in the flow chart shown in Figure 3.8.

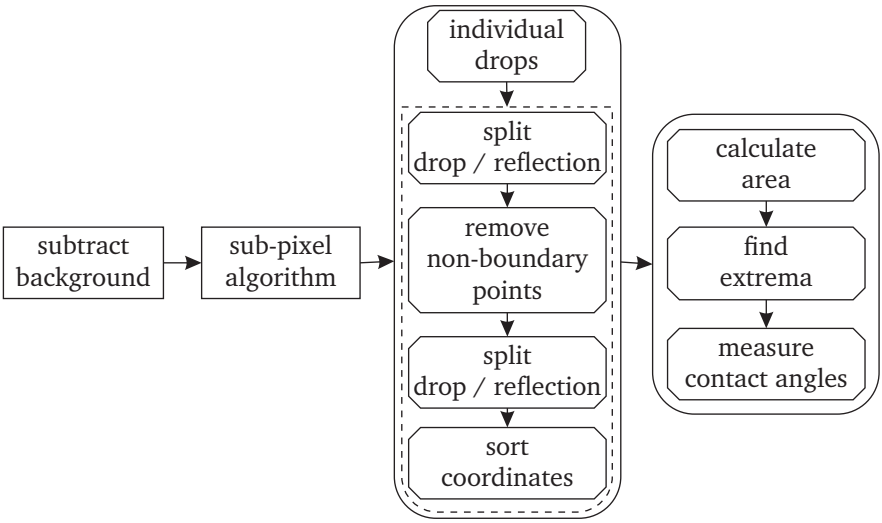

Figure 3.8: Flow chart of the image analysis algorithm.

First, a background image is subtracted from the image that should be analyzed. Next, a sub-pixel algorithm developed by Trujillo-Pino et al. (2013)

detects all gray value gradients in the image. Their algorithm does not specifically focus on detecting drop boundaries. Instead they provided a sub-pixel edge detection method for images in general. What sets their algorithm apart is that the transition from one intensity value to the next is not assumed to be continuous. Rather that a medium intensity value originates from two intensity values: one low and one high intensity. Each pixel with an intermediate value can be separated by a line into a portion with low and one with high intensity value. By doing this the boundary of an object on an image can be found with sub-pixel accuracy. Because the algorithm is not specifically tailored to shadowgraphy images of drops, five additional steps are required before the drop properties can be measured.

A check whether multiple drops have been recorded in one image is conducted and the points are separated accordingly. For each drop the points are separated into two groups, those belonging to the drop and the others belonging to its reflexion on the substrate. Next, all points that do not belong to the drop boundary are removed. The background lighting reflected within a drop is one cause for such points. Having extracted all points belonging to the boundary and reflexion a more precise splitting is done. This step is required because endocentric lenses have been used for this study. If the drop slightly moves towards or away from the focus plane the calibrated surface line looses its applicability. After cleanly separating drop boundary and reflexion the coordinates are sorted from receding to advancing contact line.

Having obtained the sorted contour coordinates, the area of the drop projection as well as the extrema of the drop are found. In this context extrema refers to the advancing and receding contact line as well as the height of the drop. Finally the contact angles for each drop are measured using a tangent method that takes the four points closest to the contact line into account.

In Figure 3.9 an analyzed image and a magnification of the advancing contact line is shown. The green lines represent the calibrated substrate surface. The detected drop contour is marked by blue points and its reflection by green ones. The red points near the tail of the drop stem from refractions of the background lighting in the drop. The measured contact angles are indicated by white lines.

The magnification clearly shows why a sub-pixel edge detection is necessary in order to minimize the errors while determining the drop contour.

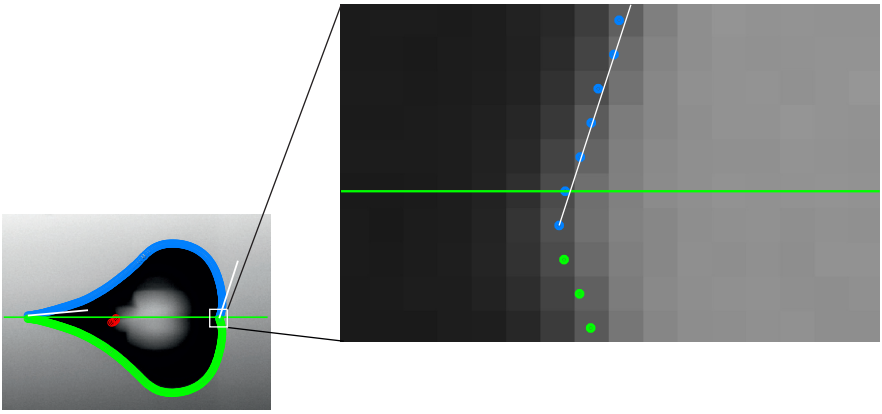

Figure 3.9: Shadowgraphy image of a 10 μl water drop on aluminum ($\Theta_{\mathrm{adv,\ cr}} = 90°$; $\Theta_{\mathrm{rec,\ cr}} = 33°$) with a 16 times magnification of the contour region of the drop. The image was recorded with a spatial resolution of $20^{\mu\mathrm{m}}/_{\mathrm{px}}$. Visible are the calibrated substrate surface (green line), detected drop contour (blue dots), its reflection (green dots), other gradients (red dots) and contact angles (white lines).

Many similar studies rely on a threshold based binarization algorithm. The measured contact angle is strongly dependent on the threshold used for the binarization. An alternative sub-pixel edge detection algorithm has been suggested by Chini and Amirfazli (2011). Their approach finds the inflection point of a function fitted to the gray value intensity. This algorithm requires significantly more computational resources and was therefore not chosen for this study.

While describing the image processing algorithm the necessity of correcting the substrate surface line was explained. In Figure 3.9 the drop moved ≈ 0.2 mm from the focus plane towards the camera. Only using the calibrated contact line in order to split the drop would have mistakenly assigned the first contour point to the reflexion. Last, the magnification shows that, due to the high resolution of the drop, the tangent method used to measure the contact angle is applicable.

4 Single drop motion

Research on wall-bounded drops, where wetting and dewetting occurs in close spatial proximity, has been the subject of multiple studies. Their motion on a substrate is always the result of a force acting on the liquid. Most commonly these forces are gravitational, aerodynamic, electric or varying substrate wettability. The topic of single drop motion is introduced with a brief overview of the published literature, placing a focus on gravity driven drop motion and aerodynamically driven drop motion, since a combination of both is often relevant for engineering applications.

From this overview two major conclusions are drawn. First, in most studies the aerodynamic forces driving the fluid are not set into relation with the actual drop. Second, no model predicting aerodynamically driven drop velocities for a certain set of parameters is available. In this chapter both are achieved, a scaling for the problem is introduced and a model predicting drop velocities is presented.

In the second part of this chapter the propagation of a drop is highlighted in greater detail. In this case slow moving drops exhibiting stick-slip behavior have been studied. This analysis, as well as a comparison with numerical results, underlines the importance of the critical advancing contact angle for aerodynamically driven drop motion.

Parts of this chapter have been published in Seiler et al. (2019). Some of the data was gathered during the Master thesis by Gloerfeld (2017).

4.1 Literature overview

Before considering gravity and shear driven drop motion, research not assignable to either category is summarized. A theoretical and numerical study on drops wetting rough surfaces was presented by Wolansky and Marmur (1999). Whereas Lu et al. (2016) studied the behavior of complex fluids, Arjmandi-Tash et al. (2017) focused on the influence of the surface properties. Gao

et al. (2017) quantified the adhesion forces between a drop held in place by a cantilever on a moving substrate. From the force on the cantilever the adhesion force can be inferred.

4.1.1 Gravity driven drop motion

Furmidge (1962) investigated the onset of drop motion on an inclined plate after deposition from a spray. He introduced a spray retention factor based on the liquid solid combination.

A structured approach was introduced by Dussan V. and Chow (1983). They introduced physical models predicting the motion of drops and bubbles.

Durbin (1988a) approached the topic of the no-slip boundary condition, as introduced in Section 2.3.1, by considering slender drops. They introduced a yield stress boundary condition.

Pierce et al. (2008) observed the sliding behavior of drops on an inclined plate. They found that the placement method of the drops as well as the experimental procedure impacts said behavior.

Chini et al. (2013) focused their work on the adhesion forces depending on an accurate contact line shape. They developed a new technique to measure the contact line shape (Chini and Amirfazli, 2011).

4.1.2 Aerodynamically driven drop motion

An early study by Durbin (1988b) discussed the aerodynamic forces acting on a drop. The required force to dislodge the drop was the main focus of his research. Many other researchers focused on this incipient motion, for instance Mahé et al. (1988) investigated the incipient motion of sessile drops using a liquid-liquid-solid system. They investigated the influence of surfactants on the wetting behavior. Milne and Amirfazli (2009) experimentally investigated the dislodging of drops due to aerodynamic forces on various surfaces. They used a flat plate in a closed return wind tunnel for their investigations. Using a similar setup, Roisman et al. (2015) considered the temperature influence and derived an analytical model allowing the critical gas flow velocity to be predicted.

The drop shape during incipient motion on chemically homogeneous surfaces was observed by Fan et al. (2011).

Fu et al. (2014) used a wind tunnel with similar flow conditions as used in this work to determine the deformation of sessile aerosol droplets on various surfaces. The incipient motion due to the turbulent aerodynamic flow was observed too.

Currently the research group of Janoske (Burgmann et al., 2018a,b; Barwari et al., 2018) concentrate their experimental efforts on the internal flow of a drop moving due to turbulent shear forces. They identified different types of drop motion: incipient motion, creeping motion and constant drop motion. Investigation of water and aqueous glycerol mixtures on different surfaces in a air channel flow were made.

Besides the experimental work outlined here, multiple numerical studies are available on shear driven drop behavior. Schleizer and Bonnecaze (1999) used a numerical boundary-integral method to determine the shape of a drop at the point of incipient motion. Incipient drop motion at low Reynolds number shear flow was studied numerically by Dimitrakopoulos and Higdon (1997). Cristini and Tan (2004) reviewed numerical methods applied to droplets in complex flows. A thesis combining numerical simulations and experiments on drop shedding through shear flow was published by Moghtadernejad (2014).

4.2 Experimental parameters

For this work drop motion on four substrates: varnished aluminum, varnished steel, aluminum and a polymethyl methacrylate (PMMA) sample, is observed using a high-speed video system. The drop propagation velocity is measured for drop volumes between $5 - 30$ μl and different flow velocities. Then an appropriate scaling for the drop velocity is proposed. This scaling is based on the dimensionless attack velocity (velocity at a distance from the wall comparable to the drop height) and on the capillary number of the drop motion. This scaling allows all the experimental results to be presented as a single curve, taking into account the wetting properties of the substrate.

The wetting properties of the substrates were measured using a Krüss DSA100 contact angle device and are given in Table 4.1.

Table 4.1: Wetting properties for the surfaces used in the experiments: advancing Θ_{adv} and receding Θ_{rec} contact angles, the hysteresis $\Delta\Theta = \Theta_{\mathrm{adv}} - \Theta_{\mathrm{rec}}$, as well as the predicted critical capillary number $\mathrm{Ca}^{\star}$ corresponding to zero receding dynamic contact angle (see Section 2.3.4).

Surface	Θ_{adv}	Θ_{rec}	$\Delta\Theta$	$\mathrm{Ca}^{\star}$
Aluminum	93°	33°	60°	2.8×10^{-3}
Varnished aluminum	73°	36°	37°	3.5×10^{-3}
Polymethyl methacrylate	71°	46°	25°	7.0×10^{-3}
Varnished steel	90°	30°	60°	2.1×10^{-3}

4.3 Constant drop motion

Having introduced the relevant literature as well as experimental parameters the first part of the study on single drop motion is presented. It focuses on the constant mean drop velocities driven by constant gas flow velocities. It begins by outlining the measurement of drop position and velocity. Continues by introducing an appropriate scaling of the gas flow and drop velocities. It ends by presenting a model describing the drop translation as a function of the attack velocity.

4.3.1 Measurements of the drop position and velocity

The motion of the drop can be quantified by its position x_{drop} and velocity v_{drop}. The value of $x_{\mathrm{drop}}(t)$ is determined by the coordinate of the mean point between the advancing and receding contact line. The velocity $v_{\mathrm{drop}} = \mathrm{d}x_{\mathrm{drop}}/\mathrm{d}t$ is obtained by numerical differentiation of $x_{\mathrm{drop}}(t)$ with time. Before this numerical differentiation, the drop position values are smoothed by a rolling average which takes the values of one-tenth of a second into account. This is required in order to reduce the noise arising from the boundary detection algorithm. In Figure 4.1 the mean channel flow velocity $\bar{U}_{\mathcal{H}}$ is shown as a dotted curve and the position of the drop in the streamwise direction as a line plot, both as a function of time. Before each experiment the substrate is thoroughly cleaned and a drop is place onto it using a Eppendorf Research plus pipette. Then the experimental process is started. The flow velocity first increases and at some instant reaches a

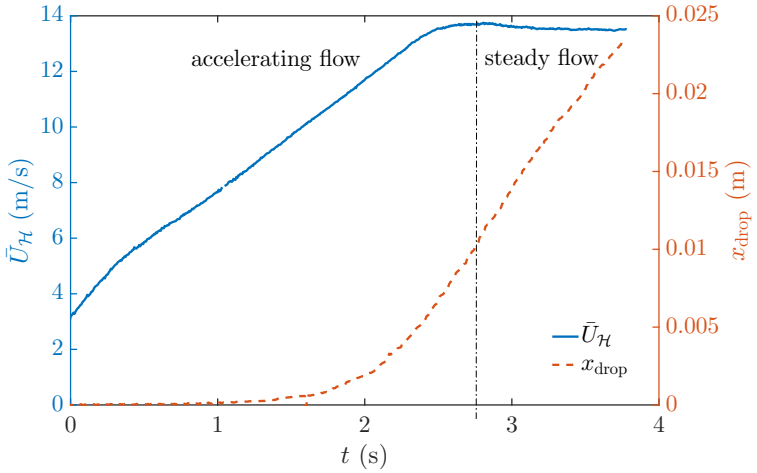

Figure 4.1: Exemplary experimental results for drop location x_{drop} substrate and mean flow velocity $\bar{U}_{\mathcal{H}}$ over time t for a 15 μl. The stages for the accelerating air flow and for the steady air flow are indicated. (Reprinted from Seiler et al. (2019), with permission of © 2019 APS Physical Review Fluids.)

nearly constant value. Once the gas flow reaches a critical velocity the drop dislodges, in this case at $t \approx 1$ s. After an initial acceleration at $t > 2.5$ s the drop starts moving downstream with a constant velocity. For $t > 5$ s both the flow velocity and drop velocity reach nearly constant values. In this work only the period for which the gas flow velocity and drop velocity are constant is considered. The symbols in Figure 4.1 highlight these conditions. These measured constant values are used for modeling the drop velocity as a function of the *attack* velocity, defined below.

In Figure 4.2 the drop velocity v_{drop} on a PMMA surface is plotted as a function of the mean flow velocity $\bar{U}_{\mathcal{H}}$ for three different drop volumes. The drop velocity increases for higher drop volumes, due to the increased drop projected area A exposed to the flow.

A comparison of the propagation velocity of a 5 μl drop on the four different surfaces is shown in Fig. 4.3. Here again the difference in the magnitude of the drop velocity is caused by the different drop shapes. For the same drop volume the projected area A is larger for drops on hydrophobic surfaces, leading to increased aerodynamic forces; thus, to higher drop velocities.

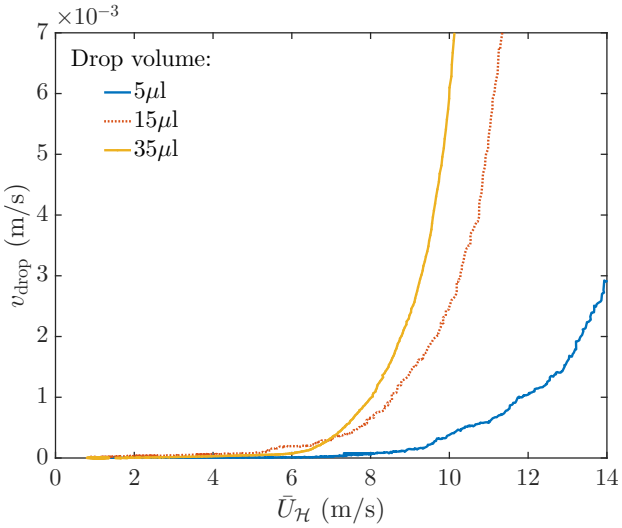

Figure 4.2: Drop velocity v_{drop} on a PMMA substrate as a function of the mean air flow velocity $\bar{U}_{\mathcal{H}}$ for different drop volumes. (Reprinted from Seiler et al. (2019), with permission of © 2019 APS Physical Review Fluids.)

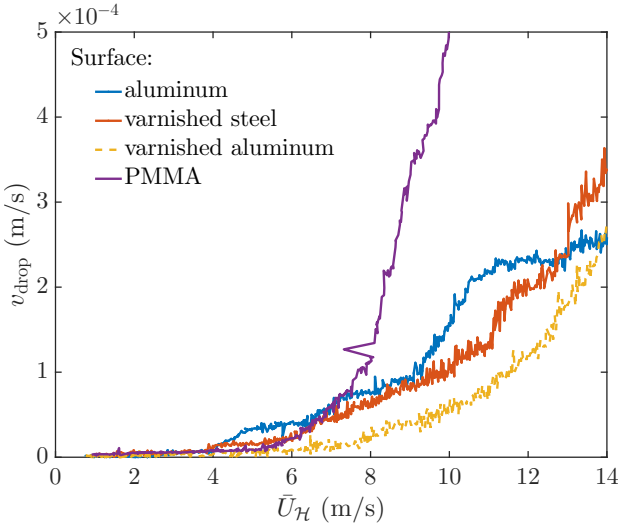

Figure 4.3: Drop velocity v_{drop} as a function of the mean flow velocity $\bar{U}_{\mathcal{H}}$ for a 5 μl drop. Properties of the substrates are listed in Table 4.1. (Reprinted from Seiler et al. (2019), with permission of © 2019 APS Physical Review Fluids.)

4.3.2 Scaling of the problem

The scaling of the problem is based on the typical geometrical properties of a liquid drop, on a representative air flow velocity, designated here as the *attack* velocity, and on a balance of forces acting on the drop.

Characteristic geometrical values. The drop velocity depends on numerous factors, one of which is the drop shape and size. The main drop dimensions are defined in Fig. 4.4. For simplicity the drop shape is first approximated by a truncated sphere with the contact angle equal to the average of the advancing and receding contact angles of the corresponding substrate

$$\overline{\Theta} \equiv \frac{\Theta_{\mathrm{adv}} + \Theta_{\mathrm{rec}}}{2}. \tag{4.1}$$

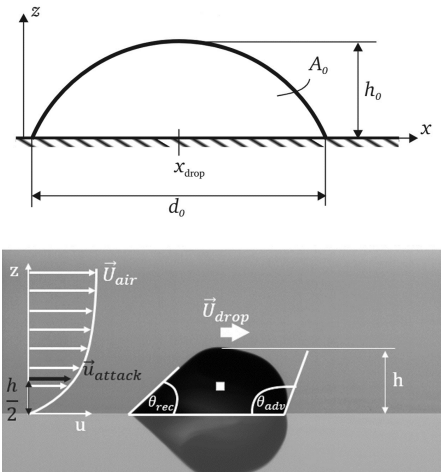

Figure 4.4: Definition of the main geometrical scales and of the *attack* velocity: (a) drop shape approximated by a truncated sphere; (b) near-wall velocity profile in the channel and the *attack* velocity. (Reprinted from Seiler et al. (2019), with permission of © 2019 APS Physical Review Fluids.)

This approximation is valid for drop sizes smaller than the capillary length and for an aerodynamically induced pressure much smaller than the capillary pressure. The drop shape deforms significantly under action of a strong enough air flow. Nevertheless, these static values will be used as characteristic sizes.

The characteristic drop height h_0, characteristic wetted diameter d_0 and the characteristic projected area A_0 can be determined for a given drop volume V_{drop} and average contact angle $\overline{\Theta}$ from the considerations of the drop geometry, as shown in Figure 4.4(a)

$$h_0 = \left[\frac{6V_{\text{drop}}\sin^2\frac{\overline{\Theta}}{2}}{\pi\left(2+\cos\overline{\Theta}\right)}\right]^{1/3}, \tag{4.2}$$

$$d_0 = 2h_0\cot\frac{\overline{\Theta}}{2}, \tag{4.3}$$

$$A_0 = h_0^2\frac{\overline{\Theta}-\sin\overline{\Theta}\cos\overline{\Theta}}{(1-\cos\overline{\Theta})^2}. \tag{4.4}$$

Characteristic velocity of the outer flow. The maximum flow velocity in the channel is not a relevant parameter influencing the drop motion, since the drop height is much smaller than the channel height and in many cases it is smaller than the height of the near-wall boundary layer. In the present work $h_0/\mathcal{H} < 1/10$. The drop is exposed to flow velocities in the vicinity of the wall, which are representative of the channel velocity at the drop height. Therefore, in the present analysis the flow velocity u_{attack} at a distance $h_0/2$ from the wall is taken as a characteristic flow velocity. This velocity, defined in Figure 4.4(b), is designated *attack* velocity. Such a definition leads to a significant simplification of the problem since the exact solution depends on the entire velocity profile near the wall. Nevertheless, is is assumed that the *attack* velocity represents well the characteristic, average air flow in the integral sense.

Using this definition, the critical flow velocity associated with incipient drop motion can be estimated from the balance of the aerodynamic driving force $F_{\text{aero}} \sim \varrho_{\text{g}} u^2_{\text{incipient}} A_0/2$ and the force associated with the contact angle hysteresis, $F_\sigma \sim \sigma d_0$, Dussan V. and Chow (1983); Pilat et al. (2012); Milne and Amirfazli (2009); Roisman et al. (2015). The expression for the estimated aerodynamic force is based on the observations that the drag coefficient is comparable with unity and is almost constant in the range of the Reynolds numbers of the flow, $10^3 < Re < 10^5$, typical for these experiments Ganser (1993).

The dimensionless *attack* velocity $\tilde{u}_{\text{attack}}$ is defined as a ratio of the *attack* velocity u_{attack} and the critical velocity associated with the drop incipient

motion. This scaling yields

$$\tilde{u}_{\text{attack}} = u_{\text{attack}} \left[\frac{\varrho_g A_0}{\sigma d_0} \right]^{1/2}, \tag{4.5}$$

where the values of d_0 and A are determined in Eq. (4.3) and (4.4).

Viscous forces in the moving drop. The viscous forces in the propagating liquid drop can be estimated by

$$F_\mu \sim \mu v_{\text{drop}} d_0^2 / h_0. \tag{4.6}$$

A typical value for this forces can be roughly estimated for a 10 μl drop on an aluminum surface. Taking $v_{\text{drop}} \sim 10^{-4}$ m/s, $d_0 \sim h_0 \sim 10^{-3}$ m, and $\mu \sim 10^{-3}$ Pa $\cdot$ s yields the force $F_\mu \sim 10^{-8}$ N. The aerodynamic force acting on this drop can be estimated for the attack velocity $u_{\text{attack}} \sim 10$ m/s as

$$F_{\text{aero}} \sim \rho_g u_{\text{attack}}^2 d_0^2 \sim 10^{-4} \text{ N}. \tag{4.7}$$

In the present study the estimated values of the viscous forces F_μ are three to four orders of magnitude smaller than the aerodynamic drag and the capillary forces. The viscous forces in the bulk drop flow can therefore be neglected in the force balance of the drop.

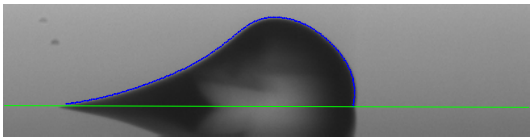

Figure 4.5: Shadowgraphy image of a 10 μl drop on aluminum substrate. The blue line indicates the detected contour of the drop and the green line represents the ground level.

However, the viscous drag forces need to be considered in a very thin drop tail formed in the receding part of the propagating drop (frontal to the air flow). Such a tail is clearly visible on the exemplary shape in Fig. 4.5. The flow in the tail can be analyzed in the long-wave approximation framework (Oron et al., 1997). For very small receding contact angles and a stationary tail shape the evolution equation of the thin film in the coordinate system fixed at the moving contact line yields

$$\sigma h_{,xxx} + \frac{3\tau_g}{2h} - \frac{3\mu v_{\text{drop}}}{h^2} = 0, \tag{4.8}$$

where τ_g is the aerodynamic shear stress at the wall, v_{drop} is the drop propagation velocity, and x is the coordinate in the direction of the drop propagation. The equation is singular at the contact line, therefore it is applicable only to the outer region of the corner flow near the receding contact line.

The evolution equation (4.8) can be written in dimensionless form using h_T as a thickness scale and λ as a length scale for x

$$h_T = \frac{3^{2/3}\mu^{2/3}v_{\text{drop}}^{2/3}}{\kappa\sigma^{2/3}}, \quad \lambda = \left[\frac{3\mu v_{\text{drop}}}{\kappa^3\sigma}\right]^{1/3}, \tag{4.9}$$

where κ is the characteristic liquid film curvature estimated through

$$\kappa \sim \varrho_g u_{\text{attack}}^2/\sigma. \tag{4.10}$$

The dimensionless aerodynamic shear stress is obtained in the form

$$T = \frac{3^{2/3}}{2}\tau_g\mu^{-1/3}\sigma^{-2/3}\kappa^{-1}v_{\text{drop}}^{-1/3}. \tag{4.11}$$

The expression for T can be simplified

$$T = \frac{3^{2/3}\tau_g}{2\varrho_g u_{\text{attack}}^2}\text{Ca}^{-1/3}, \tag{4.12}$$

where the capillary number, defined in (2.1), is based on the drop propagation velocity v_{drop}.

The dimensionless evolution equation for the drop tail is obtained from (4.8) in the following form

$$H_{;XXX} + \frac{T}{H} - \frac{1}{H^2} = 0, \tag{4.13}$$

where the dimensionless thickness and x-coordinate are defined as

$$H = \frac{h}{h_T}, \quad X = \frac{x}{\lambda}. \tag{4.14}$$

In the present experiments wall shear stresses are obtained from static pressure loss in the streamwise direction. The shear stress is $\tau_g \sim 1$ Pa.

The value of T, estimated using (4.12), is of order $T \sim 10^{-4}\text{Ca}^{-1/3}$. As a result, T is much smaller than unity if $\text{Ca} > 10^{-6}$. The motion of the drop

becomes observable if the capillary number $\mathrm{Ca} \gg 10^{-6}$. This condition is fulfilled for all of our experiments and the effect of the shear stresses in the gas flow on the shape of the drop tail and on the viscous force is negligibly small.

The term including T in Eq. (4.13) can thus be neglected and the equation becomes self-similar.

$$H_{,XXX} - \frac{1}{H^2} = 0, \quad T \ll 1. \tag{4.15}$$

The viscous force applied to the tail part can be estimated as

$$F_{\mathrm{tail}} \sim \frac{\mu v_{\mathrm{drop}}}{h_T} \lambda d_0 = \frac{d_0}{\sqrt[3]{3}} \mu^{2/3} \sigma^{1/3} v_{\mathrm{drop}}^{2/3} \tag{4.16}$$

Balance of forces applied to the moving drop.

The force balance of the moving drop can be now written in the form

$$F_{\mathrm{tail}} = F_{\mathrm{aero}} - F_\sigma = \frac{\varrho_g}{2} u_{\mathrm{attack}}^2 A_0 - \frac{\varrho_g}{2} u_{\mathrm{incipient}}^2 A_0. \tag{4.17}$$

This equation is based on the assumption that the dependence of the adhesion force F_σ on the drop propagation velocity v_{drop} is negligibly weak.

The balance of forces (4.17) with the help of the expression for the viscous force in the drop tail (4.16) yields

$$\mathrm{Ca} = K \left(\tilde{u}_{\mathrm{attack}}^2 - \tilde{u}_{\mathrm{incipient}}^2 \right)^{3/2}, \tag{4.18}$$

where the dimensionless parameters K and $\tilde{u}_{\mathrm{incipient}}$ are determined only by the substrate wettability and roughness properties.

Equation (4.18) is valid for $\tilde{u}_{\mathrm{attack}} \geq \tilde{u}_{\mathrm{incipient}}$.

In this work, the values of $\tilde{u}_{\mathrm{incipient}}$ for different substrates are obtained by fitting the experimental data for capillary number Ca using the expression (4.18). The estimated values of $\tilde{u}_{\mathrm{incipient}}$ are listed in Table 4.2. It is important that the estimated values of $\tilde{u}_{\mathrm{incipient}}$ are comparable with unity. This means, that the main forces governing the drop propagation along a solid substrate are accounted for in this work.

Table 4.2: Dimensionless *attack* velocity $\tilde{u}_{\text{incipient}}$ corresponding to the apparent inception of drop motion on different surfaces, determined by fitting the experimental data.

Surface	$\tilde{u}_{\text{incipient}}$
Aluminum	1.13
Varnished aluminum	1.11
Polymethyl methacrylate	1.10
Varnished steel	1.18

4.3.3 Velocity of drop translation as a function of the attack velocity

To validate the form of the expression (4.18) the values of $\text{Ca}^{2/3}$ calculated from the measured velocities of drop translations are shown in Fig. 4.6 as a function of $(\tilde{u}^2_{\text{attack}} - \tilde{u}^2_{\text{incipient}})$. It is remarkable that the points corresponding to various substrates and various drop volumes almost collapse onto one curve. Some scatter is observed for drop motion over the same substrate. The scatter is the result of strong drop oscillations caused by propagation of capillary waves along the drop interface as well as a heterogeneity of the investigated substrates.

Moreover, as predicted in (4.18), the value of $\text{Ca}^{2/3}$ increases almost linearly with the value of $(\tilde{u}^2_{\text{attack}} - \tilde{u}^2_{\text{incipient}})$ if $\text{Ca}^{2/3} < 0.02$. The estimated coefficient K, defined in (4.18), is nearly the same for all the investigated substrates, $K = 0.0011$.

For the range $(\tilde{u}^2_{\text{attack}} - \tilde{u}^2_{\text{incipient}}) > 1.5$ the linear dependence is no longer given and the capillary numbers reach a saturated plateau value in the range $0.015 < \text{Ca}^{2/3} < 0.02$, which corresponds to $1.8 \times 10^{-3} < \text{Ca} < 2.8 \times 10^{-3}$. It is interesting that these plateau values are comparable with the values of the critical capillary number of dewetting, $\text{Ca}^{\star}$, listed in Table 4.1. At higher gas flow velocities the drops break up. These cases are not considered in the present work.

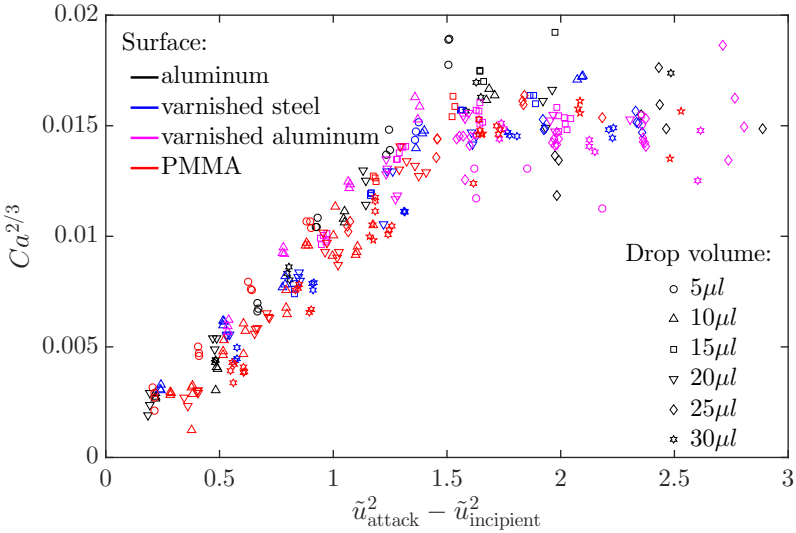

Figure 4.6: Capillary number of a steady moving drop as a function of the dimensionless *attack* velocity for different substrates and drop volumes. The values of $\tilde{u}_{\text{incipient}}$ for each substrate are obtained by the fitting with the experimental data and are listed in Table 4.2. (Reprinted from Seiler et al. (2019), with permission of © 2019 APS Physical Review Fluids.)

4.4 Drop propagation

Having introduced a model based on time averaged velocities a more detailed study of the drop motion was conducted. For this high speed images, as described in Section 3.3, were recorded at 4000 fps. The high temporal and spatial resolution allowed observation of the contact lines and angles in greater detail. During this analysis two distinct propagation types have been found. As before, only experiments with constant mean velocities (Section 4.3.1) were considered.

4.4.1 Propagation types

Even though the drops moved with a constant mean velocity two different motion types could be discerned. The first, both contact lines moved

throughout the motion. The second, the drops propagated in a stick-slip motion where the advancing and receding contact lines pinned intermittently.

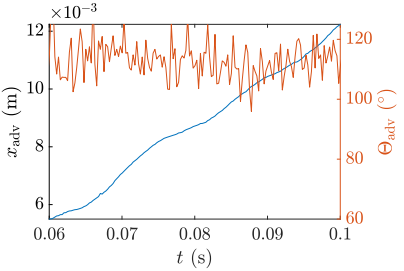

(a) Continuous drop propagation $\tilde{u}_{att} = 1.619$; $Ca = 2.2 \times 10^{-3}$

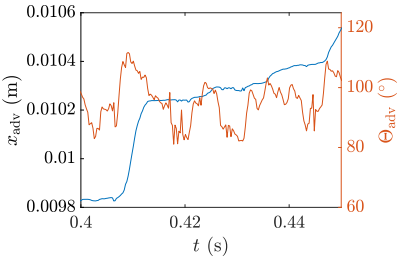

(b) Stick-slip drop propagation $\tilde{u}_{att} = 1.426$; $Ca = 2.7 \times 10^{-4}$

Figure 4.7: Diagram showing the position of the advancing contact line, $x_{adv.}$ and current advancing contact angle Θ_{adv} over time, t. 10 μl drops were moved over an aluminum substrate ($\Theta_{adv,\ cr} = 93°$; $\Theta_{rec,\ cr} = 33°$).

In Figure 4.7 both types of motion are shown. The blue lines in both plots represent the contact line position over time. In a) it constantly moves with only minor changes in its velocity. In contrast, the motion of the advancing contact line in b) is interrupted by it pinning at one position. In both graphs the red lines represent the corresponding advancing contact angle. In case a) it always stays above 100° even though an oscillation is present. For b) the oscillation occurs between 80° and 120°.

The conditions and influencing factors separating both propagation types has yet not been found with the available data. From the experiments as well as the presented data it is apparent that the stick-slip behavior of a drop only occurs at small Ca numbers. In Figure 4.7 one order of magnitude lies between both mean drop velocities. Barwari et al. (2018) described the stick-slip propagation as creeping motion.

4.4.2 Dynamic critical contact angle

The stick-slip motion of a drop is due to its nature very useful when analyzing the critical contact angle. While the contact line is pinned, the contact angle lies below its critical advancing value. When the contact line motion resumes the critical angle is exceeded.

A relation between motion and contact angle is found by cross-correlating the binarized velocity and contact angle. All steps necessary for this data analysis are outlined in the following.

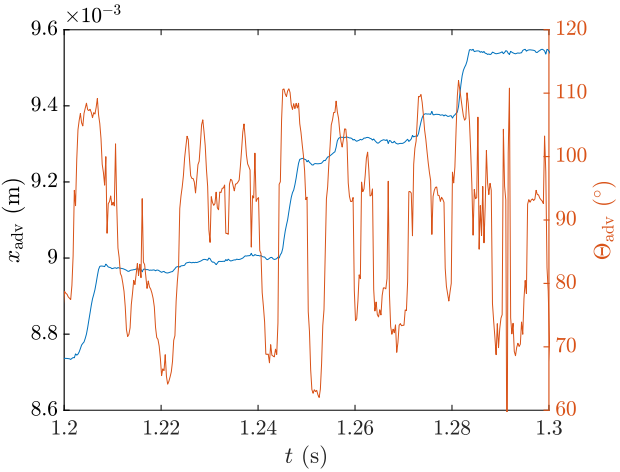

Figure 4.8: Diagram showing the position of the advancing contact line, $x_{\text{adv.}}$ and advancing contact angle Θ_{adv} over time, t. 10 μl drop on PMMA ($\Theta_{\text{adv, cr}} = 71.5°$; $\Theta_{\text{rec, cr}} = 46°$). $\tilde{u}_{\text{att}} = 1.36$; $\text{Ca} = 1.06 \times 10^{-4}$

The temporal progression of contact line position, x_{adv} and contact angle Θ_{adv} are shown in Figure 4.8. In order to ensure readability of the plots, an exemplary time frame of $\Delta t = 0.1$ s is shown. PMMA was chosen as a substrate, because water drops exhibited the stick-slip motion on this surface most prominently of all the investigated substrates.

By applying a forward differentiation to x_{adv}, the contact line velocity, v, was calculated, as is shown in Figure 4.9. Next, the velocity and contact angle were binarized using threshold values. All velocities and angles below the thresholds were treated as zero and above them as one. Considering the accuracy of the image analysis algorithm, a velocity threshold $\epsilon_v = 0.03$ m/s was chosen. The result of this binarization is shown in Figure 4.10. The threshold $\epsilon_\Theta = 105.9°$ was selected for this plot, because it led to the highest correlation between velocity and angle. The following paragraphs and figures will further highlight this.

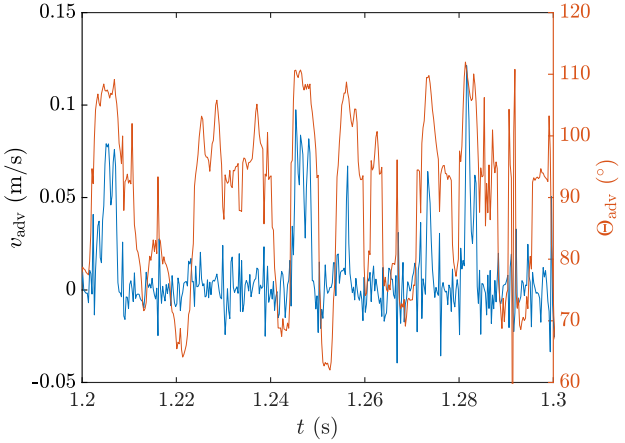

Figure 4.9: Diagram showing the advancing contact line velocity, $v_{\text{adv.}}$ and advancing contact angle Θ_{adv} over time, t. 10 μl drop on PMMA ($\Theta_{\text{adv, cr}} = 71.5°$; $\Theta_{\text{rec, cr}} = 46°$). $\tilde{u}_{\text{att}} = 1.36$; $\text{Ca} = 1.06 \times 10^{-4}$

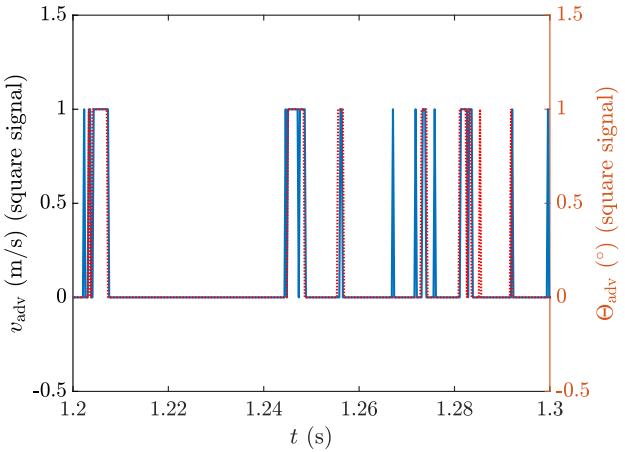

Figure 4.10: Diagram showing the square signal of the advancing contact line velocity, $v_{\text{adv.}}$ and square signal of the advancing contact angle Θ_{adv} over time, t for the motion shown in Fig. 4.8. Binarization threshold values: $\epsilon_\Theta = 105.9°$; $\epsilon_v = 0.03$ m/s

The result of the cross-correlation (Bendat and Piersol, 2011) for these conditions is shown in Figure 4.11. τ is the lag-time shift of the correlation, $R_{\Theta_{\mathrm{adv}},v_{\mathrm{adv}}}$ is the correlation value lying between -1 and 1. At $\tau = 0$ s the highest correlation of $R_{\Theta_{\mathrm{adv}},v_{\mathrm{adv}}} = 78\%$ was calculated, indicating that no time delay is present between the angle exceeding the threshold value and the contact line moving.

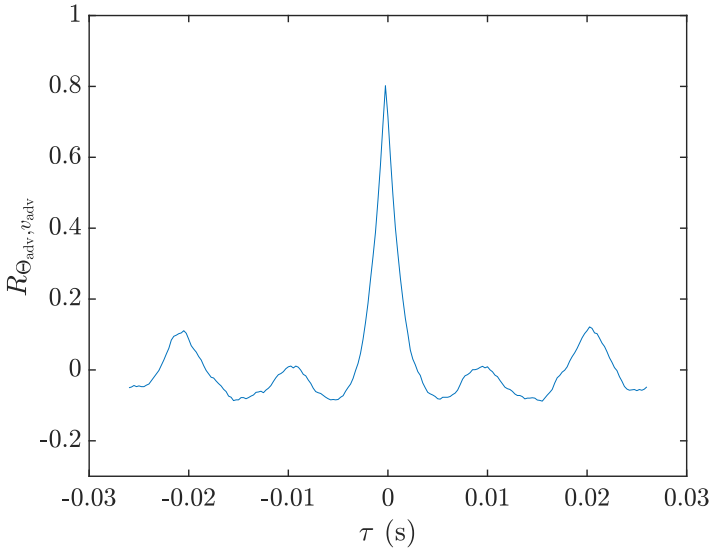

Figure 4.11: Cross correlation between both square signals shown in Fig. 4.10. $\epsilon_\Theta = 105.9°$

Using this method to cross-correlate contact angle and contact line velocity, a variation of the contact angle threshold ϵ_Θ was conducted. A plot of the maximum correlation value and the threshold angle is shown in Figure 4.12. The highest correlation value was always found for $\tau = 0$ s. ϵ_Θ was varied from $\Theta_{\mathrm{adv,\ cr}}$ to the highest measured contact angle in the experiment. At $\Theta_{\mathrm{adv,\ cr}}$, measured by slowly inflating a drop, a correlation of only $R_{\Theta_{\mathrm{adv}},v_{\mathrm{adv}}} = 118\%$ was calculated with this method. The highest correlation value $R_{\Theta_{\mathrm{adv}},v_{\mathrm{adv}}} = 78\%$ was determined for $\epsilon_\Theta = 105.9°$. The validity of this correlation approach is supported by the behavior observable at 1.22 s $< t <$ 1.24 s. The contact line pinnes while $\Theta_{\mathrm{adv,\ cr}} << \Theta_{\mathrm{adv}} \approx 100°$.

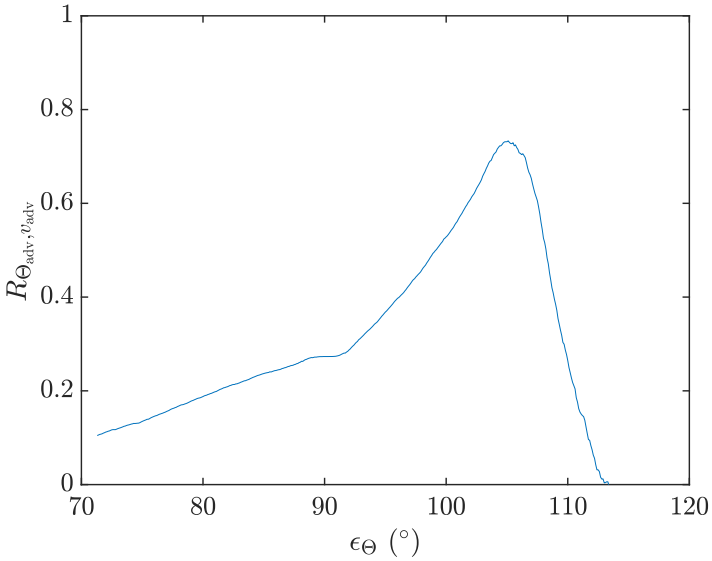

Figure 4.12: Maximum value of correlation between both signals over varying ϵ_Θ value.

4.5 Comparison with numerical simulation

One of the goals of this work was to provide validation data for numerical simulations. A study by Rettenmaier (2019) approached the topic of wall-bounded drop motion numerically, extended the volume of fluid openFOAM solver and ran simulations for his thesis. In this work he implemented multiple surface tension and wetting models. He specifically focused on the contact line dynamics and contact angle hysteresis as well as on dynamic mesh refinement and load balancing. For the turbulence in the channel flow he used a hybrid turbulence model, combining: Reynolds averaged Navier Stokes methods (RANS) and large eddy simulation methods (LES). In order to validate the implemented models and solver he used experimental results from the present study. Further details on the numerical methods as well as set-up can be found in his thesis.

Using the example of a $V_{\text{drop}} = 25$ μl water drop on PMMA, the validation of the solver is presented. The simulation was setup analog to the experiment. Further details on the experimental procedure can be found in Section 4.3.1. For each experiment a drop has been placed on the substrate, while the wind tunnel was turn off. After the pipette has been retracted the flow was linearly accelerated at a rate of $\dot{\text{Re}}_{\mathcal{H}} = 3758$ 1/s. At a critical flow velocity the sessile drop dislodged and began its downstream motion.

For the simulation, the gas flow inside the wind tunnel has been initialized at a Reynolds number $\text{Re}_{\mathcal{H}} = 3 \times 10^3$. Having a stable turbulent gas flow in the simulated test section a sessile drop was added and the simulation was run long enough for the system to settle. After an equilibrium state was reached, the simulated flow was accelerated in the same way as it was in the experiments.

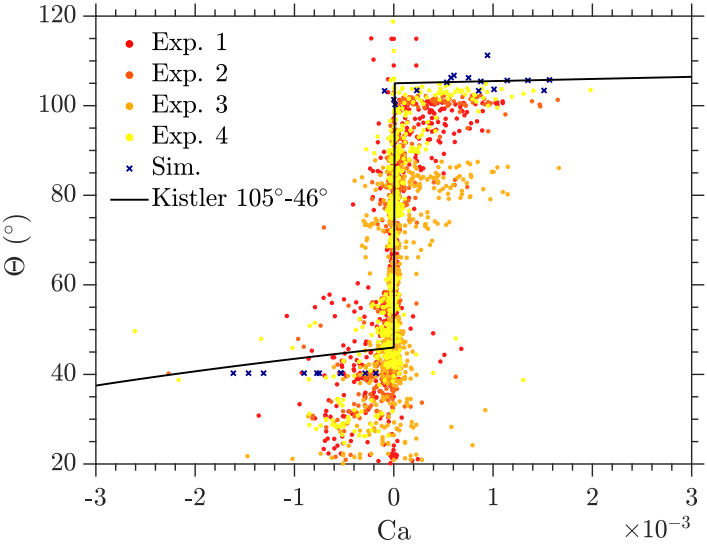

Figure 4.13: Diagram comparing numerical and experimental results of a $V_{\text{drop}} = 25$ μl on PMMA. Capillary number Ca is plotted on the ordinate and Θ on the abscissa. The data with positive Ca numbers belongs to the advancing contact line and angle, the negative ones to the receding side. For the simulation $\Theta_{\text{adv,cr}} = 105°$ and $\Theta_{\text{res,cr}} = 46°$ were used as boundary conditions.

For the numerical solver the wetting properties of the substrate are represented by the critical advancing and receding contact angles. The importance of this boundary condition is discussed in greater detail in the work of Rettenmaier (2019). In this case $\Theta_{\mathrm{adv,cr}} = 105°$ and $\Theta_{\mathrm{res,cr}} = 46°$ were used as boundary condition values for the simulation. The Ca-Θ diagram comparing experimental and numerical results as well as the empirical Kistler curve is shown in Figure 4.13. Looking at the advancing side of the diagram it can be seen that the implemented algorithm reproduces as expected the empirical Kistler curve. The experimental results greatly accumulate around 105°, nearly the angle for which the best cross-correlation was found (Section 4.4.2).

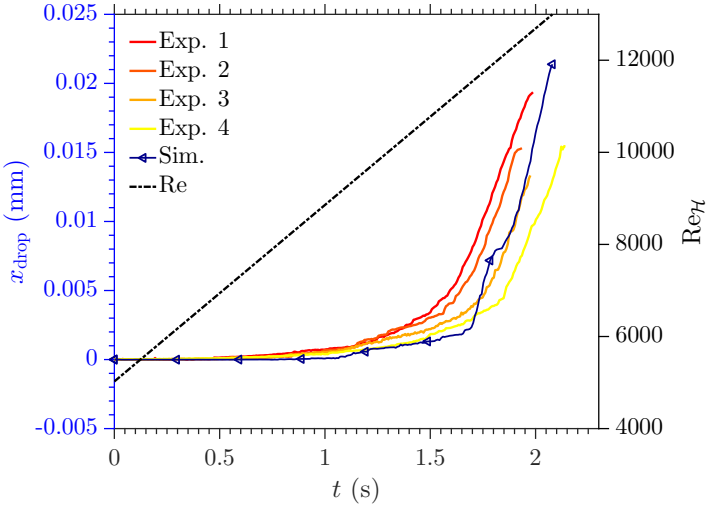

Figure 4.14: Diagram comparing numerical and experimental results of a $V_{\mathrm{drop}} = 25\ \mu\mathrm{l}$ on PMMA. Time t is plotted on the abscissa and x_{drop} and $\mathrm{Re}_{\mathcal{H}}$ on the ordinates.

For the same set of data a diagram plotting the drop position x_{drop} and channel Reynolds number $\mathrm{Re}_{\mathcal{H}}$ over time t is shown in Figure 4.14. The data is aligned with the Reynolds number $\mathrm{Re}_{\mathcal{H},0} = 5 \times 10^3$ at $t = 0$ s. Incipient motion and initial acceleration is not identical for each experiment. These deviations can be explained by the heterogeneity of the substrate, turbulent nature of the channel flow and oscillations of the drops. Defining a threshold

of $\Delta x_{\mathrm{drop,\ im}} = 1.5$ mm allows determining the critical gas flow velocities for incipient motion. In the experiments the Reynolds numbers for incipient motion lie between $\mathrm{Re}_{\mathcal{H},\ \mathrm{im}} = 9.66 \times 10^3$ and $\mathrm{Re}_{\mathcal{H},\ \mathrm{im}} = 10.5 \times 10^3$. The simulated drop and the most similar experiment differ by only 4% in critical Reynolds number $\mathrm{Re}_{\mathcal{H},\ \mathrm{im}} = 10.97 \times 10^3$.

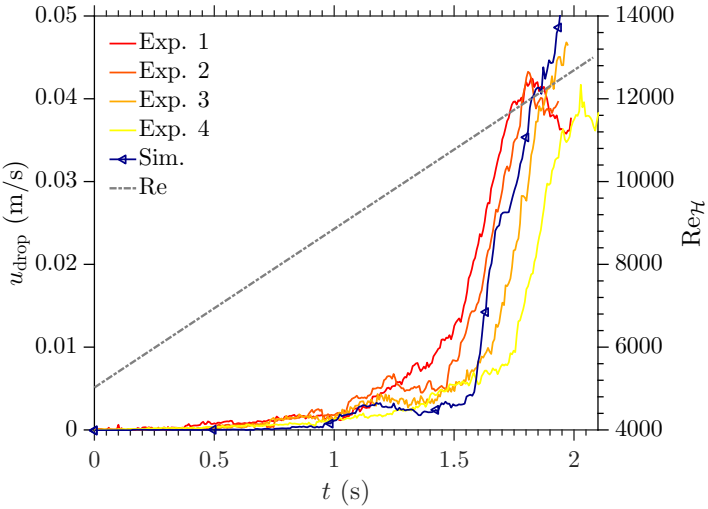

Figure 4.15: Diagram comparing numerical and experimental results of a $V_{\mathrm{drop}} = 25\ \mu$l on PMMA. Time t is plotted on the abscissa and v and $\mathrm{Re}_{\mathcal{H}}$ on the ordinates.

In Figure 4.15 a v-t diagram for the experiments and the simulation is shown. As described in Section 4.3.1 a rolling average spawning one-tenth of a second is applied to numerical and experimental data. Numerical and experimental results again compare well. The velocity plateau visible after 1 s has been described by Barwari et al. (2018) as creeping motion. In it the drop propagates in the previously introduced stick-slip motion.

Four pairs of shadowgraphy images of drops at different channel Reynolds numbers are shown in Figure 4.16. The top images were extracted from the numerical simulation and the bottom image from one of the experiments. The idea behind this qualitative comparison is to highlight that the numerically predicted drop shapes resemble those observable in reality.

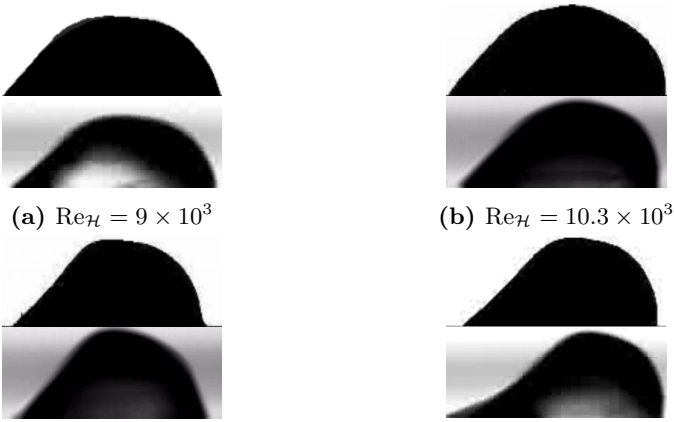

(a) $\mathrm{Re}_{\mathcal{H}} = 9 \times 10^3$ **(b)** $\mathrm{Re}_{\mathcal{H}} = 10.3 \times 10^3$

(c) $\mathrm{Re}_{\mathcal{H}} = 11.3 \times 10^3$ **(d)** $\mathrm{Re}_{\mathcal{H}} = 12.3 \times 10^3$

Figure 4.16: Comparison between numerical (top) and experimental (bottom) shadowgraphy images, highlighting the similarities in actual and simulated drop shape. Image pairs for four different channel Reynolds numbers $\mathrm{Re}_{\mathcal{H}}$ are shown.

While comparing numerical and experimental results it is noteworthy that the good agreement between both was found when using a critical advancing contact angle $\Theta_{\mathrm{adv,\ cr}} = 105°$ as boundary condition. This angle is nearly identical to the angle that has the highest correlation between velocity and contact angle as discussed in Section 4.4.2.

5 Drop-groove interaction

This section is based on a journal manuscript which is currently under review. Some of the data was gathered during the Bachelor thesis by Mayrhofer (2018).

Building on the previously introduced scaling and model predicting the motion of an aerodynamically driven individual drop, this chapter presents a study on surfaces with geometric discontinuities such as grooves or roughness elements. They are important in many practical applications, examples include air-frame icing (Tarquini et al., 2014; Theodorsen and Clay, 1933), exterior vehicular water management (Hagemeier et al., 2011), or the widely known lotus effect (Neinhuis and Barthlott, 1997; Marmur, 2004). Although there exists some controversy regarding the terminology when classifying and describing surface morphology (Stout and Blunt, 2001), in the present study the size of the surface structures is the most relevant distinguishing parameter and furthermore, only simple groove geometries are considered.

The main subject of this study is the propagation of an aerodynamically driven drop over a groove in an otherwise smooth surface. The groove dimensions are of the same order as the drop diameter; hence, it can be considered a macroscopic structure. Recently two studies (Dianat et al., 2017a,b) have numerically simulated this situation using a level-set volume of fluid approach, whereas the present study examines the problem experimentally and analytically.

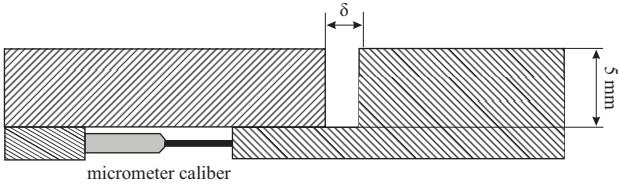

Figure 5.1: Sketch of the variable groove.

The surface used in this study consists of two aluminum plates with an advancing contact angle of $\Theta_{\text{adv, cr}} = 90°$ and a receding contact angle of $\Theta_{\text{rec, cr}} = 33°$. These angles were determined using a Krüss DSA 100 measurement system. One of the plates is fixed and the other can be traversed in the flow direction, forming a groove of variable width. The groove width, δ, is set by a micrometer caliper and the depth remains constant at 5 mm. A sketch of the groove is shown in Figure 5.1. The contact angle of the groove walls is $\Theta_{\mathcal{G}} = 70°$.

For this study the high speed shadowgraphy imaging setup, described in Section 3.3 was used. The field of view of the Phantom v12.1 camera extends 25 mm upstream and 10 mm downstream of the groove; hence, both the velocity of the drop approaching the groove as well as its behavior when encountering the groove can be determined. The same methods and measurements for the drops moving with constant velocity were used as introduced in Section 4.3.

The aim of the study is to experimentally determine under what conditions the propagating drop will be captured by the groove, or portions of the liquid will pass over the groove. This chapter is divided into three parts: First, the observable outcomes are highlighted and described. Second, an investigation of the absorption time of a stationary drop by the groove is presented. Last, the interaction of the aerodynamically driven drops and single groove are shown. Using the stationary and dynamic results, a model is then presented to predict 'capture' or 'pass', establishing the correct scaling parameters for describing the phenomenon.

5.1 Observations

The visualizations revealed three possible outcomes: only a portion of the liquid enters the groove and the rest continues propagation downstream of the groove; the drop is immediately captured by the groove; or the drop wets the downstream edge of the groove before being captured by it. Sketches of these three outcomes are shown in Figure 5.2.

A sequence of shadowgraphy images of a drop passing a groove (Figure 5.2a) are shown in Figure 5.3. At $t = 0$ s the drop approaches the groove with constant velocity. At $t = 45$ ms the advancing contact line of

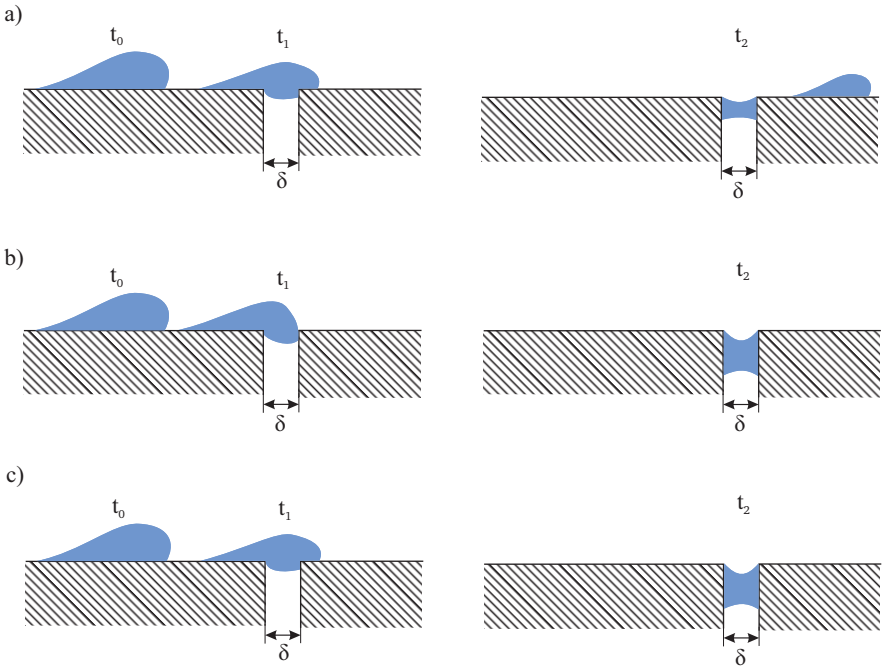

Figure 5.2: Sketch of the three outcomes a drop exhibits when encountering a groove: a) drop passes the groove b) drop is immediately captured, c) drop wets the downstream edge and is captured

the drop pins at the upstream edge of the groove. The aerodynamic force then deforms the drop over the groove ($t = 60$ ms) while the contact line is pinned at the upstream edge. Next, a new advancing contact line forms on the downstream side, as seen at $t = 75$ ms. At this point a liquid bridge between both edges has formed. The drop continues its forward motion while a fraction of the drop volume remains in the liquid bridge.

The second type of outcome, a drop being immediately captured by the groove, occurs when the substrate on the downstream side is not wetted. In this case, the combination of groove width (δ), drop volume (V_0), and drop velocity (v) either leads to the drop exclusively pinned on the upstream wall of the groove or wetting of the downstream wall while being captured.

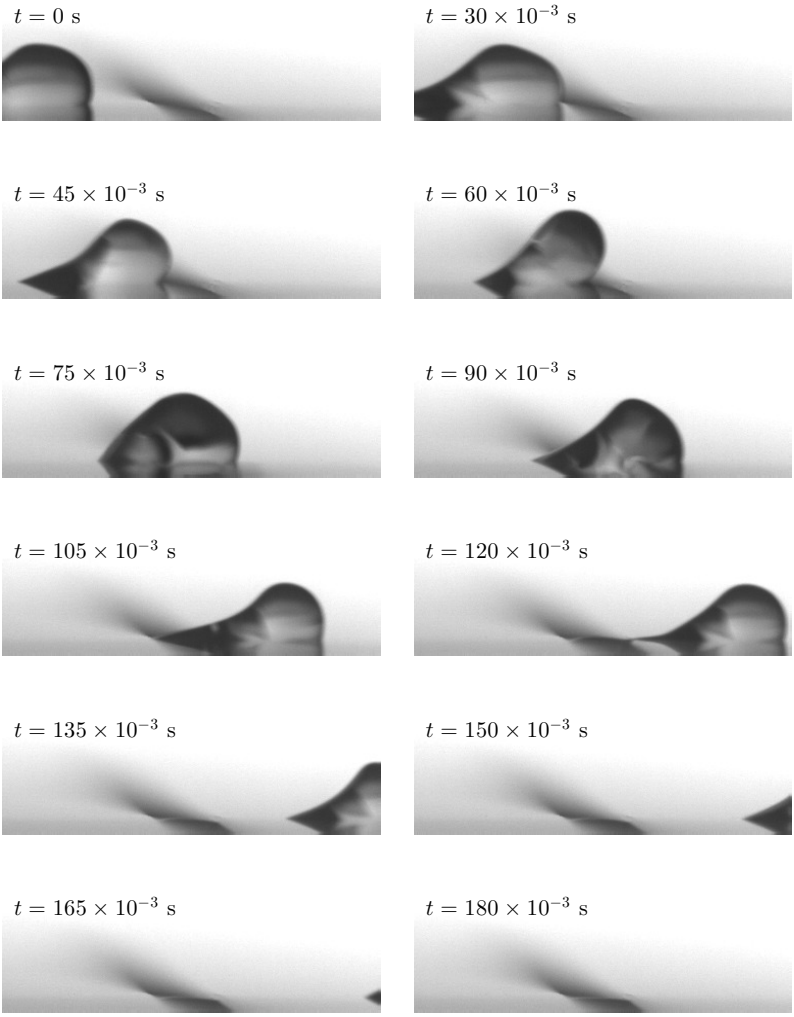

Figure 5.3: Series of shadowgraphy images showing a drop groove interaction experiment with a $V_0 = 15$ μl water drop. The groove has a width of $\delta = 1.5$ mm. The dimensionless attack velocity is $\tilde{u}_{\mathrm{att}} = 1.63$, and the capillary number is $\mathrm{Ca} = 1.9 \times 10^{-3}$

A sequence of images showing the third outcome is shown in Figure 5.4. Similar to the case where the drop passes the groove, a liquid bridge between

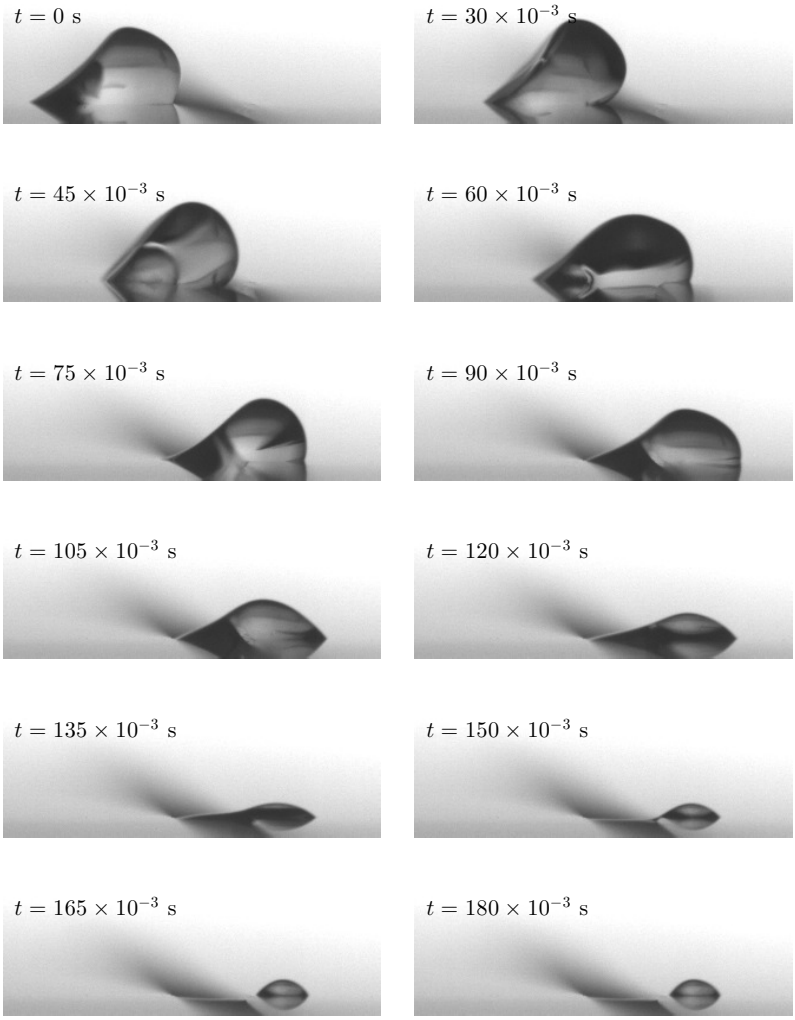

Figure 5.4: Series of shadowgraphy images showing a drop-groove interaction experiment with a $V_0 = 15$ μl water drop. The groove has a width of $\delta = 1.5$ mm. The dimensionless attack velocity is $\tilde{u}_{\mathrm{att}} = 1.57$, and the capillary number is $\mathrm{Ca} = 1.7 \times 10^{-3}$

both sides of the groove is formed. At $t = 60$ ms the majority of volume

is located over the groove while the substrate on the downstream edge has already been wetted. The capillary forces, dominating in this case, suck the drop into the groove. Since the wetted downstream distance is comparable to the groove width, as seen at $t = 9$ ms, the force does not suffice to move the contact line on the downstream side. While the drop is sucked into the groove, a small droplet remains on the downstream side of the groove. Such minor residuals may remain on both sides of the groove if the dewetting of the substrate can not keep up with the absorption rate of the groove.

5.2 Interaction of a stationary drop with a groove

When a drop interacts with a groove, part of the drop volume can be sucked into the groove by the forces associated with the groove wettability. The residual drop downstream of the groove can be pinned at the rear corner of the groove. The drop will continue to move further if the residual volume is large enough such that the aerodynamic forces applied to this residual volume is higher than the adhesion forces, associated with pinning at the groove edge.

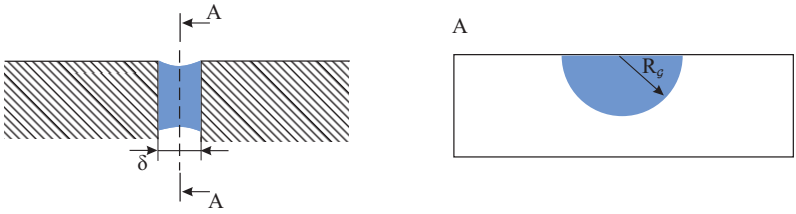

Figure 5.5: Sketch of the expanding disc during drop absorption.

In order to better understand the mechanism of the drop suction into the groove a set of experiments was performed on the suction of an initially apparently stationary drop. In the experiments a drop produced by a pipette has been gently placed centrally on the groove. The time of complete suction has been measured for various drop volumes ($V_0 = 5\ \mu$l; 10 μl; 15 μl; 20 μl) and groove thicknesses ($\delta = 0.1$ mm; 0.25 mm; 0.5 mm).

For these experiments the groove was set-up outside of the wind tunnel and a drop was placed on the groove using a Eppendorf research plus pipette. A video of the absorption was recorded using a Nikon D90 and a Zeiss 50 mm lens. From the recording, the time $t_{\mathcal{G}}$ required for the drop to be fully absorbed has been determined.

In order to estimate the suction time theoretically, the liquid bridge in the groove is approximated by an expanding disc of radius $R_{\mathcal{G}}(t)$. This approximation is based on the fact that the effect of gravity on the flow in the groove is small, and therefore all directions of flow are equal. A sketch of the expanding disc within the groove is shown in Figure 5.5.

The average radial velocity of the flow in the groove is $u_{\mathcal{G}} = \dot{R}_{\mathcal{G}} R_{\mathcal{G}}/r$, which satisfies the mass balance equation. Since the Reynolds number of the flow in the groove is much smaller than the unity, the inertial terms can be neglected and the pressure gradient can be approximated as $\partial p/\partial r \approx -12\mu u_{\mathcal{G}}/\delta^2$. This approximation is based on the parabolic velocity profile in the expanding liquid bridge. Then the expression for the pressure in the liquid bridge is obtained in the form

$$p_{\mathcal{G}} = p_0 - \frac{12\mu R_{\mathcal{G}} \dot{R}_{\mathcal{G}}}{\delta^2} \ln\left(\frac{r}{r_0}\right), \tag{5.1}$$

where r_0 is the initial radius and p_0 is the initial pressure at the boundary between the bridge and the drop. Values r_0 and p_0 must be introduced to avoid the singularity in the equations at $r = 0$.

At large distances from the drop, $r \gg r_0$, the value of the logarithmic term in (5.1) varies only weakly. Therefore, as a zero approximation this term can be expressed by a constant. For large distances from the drop therefore

$$p_{\mathcal{G}} \approx -\frac{K\mu R_{\mathcal{G}} \dot{R}_{\mathcal{G}}}{\delta^2}, \tag{5.2}$$

where K is a constant.

The pressure at the disk edge is estimated by the wettability of the groove and its thickness. The estimation, with the help of the Young-Laplace equation, yields $p_{\mathcal{G}}(r = R_{\mathcal{G}}) = -2\sigma\cos\Theta_{\mathcal{G}}/\delta$. Substitution of this boundary condition into Eq. (5.1) yields the following ordinary differential equation for $R_{\mathcal{G}}(t)$

$$R_{\mathcal{G}}(t)\dot{R}_{\mathcal{G}} = \frac{2\delta\sigma\cos\Theta_{\mathcal{G}}}{K\mu}, \tag{5.3}$$

the solution of which is

$$R_{\mathcal{G}} = \left[\frac{2\delta\sigma\cos\Theta_{\mathcal{G}}}{K\mu}t\right]^{1/2}. \tag{5.4}$$

Expression (5.4) allows estimation of the time $t_{\mathcal{G}}$ required for the complete capture of the liquid volume V_0. The radius of the bridge at this instant can be estimated from the mass balance of the drop $V_0 \approx \pi R_{\mathcal{G}}^2\delta/2$. Expression (5.4) then yields

$$t_{\mathcal{G}} \sim \frac{\mu V_0}{\delta^2\sigma}. \tag{5.5}$$

The coefficient of proportionality in the linear relation (5.5), $K/\pi\cos\theta_{\mathcal{G}}$, is of order 10^3.

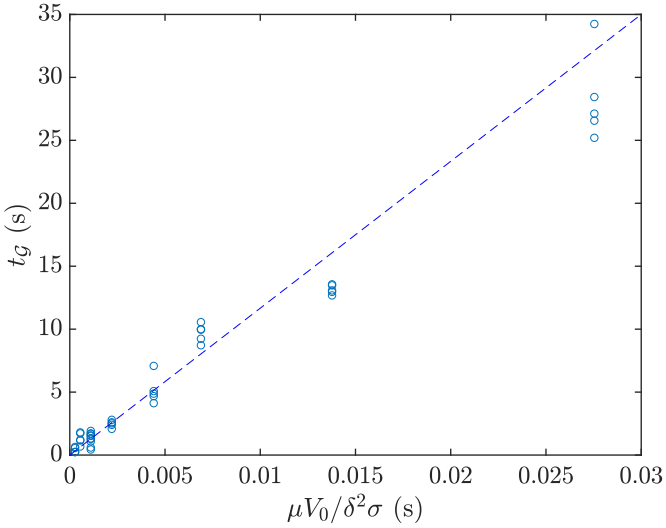

Figure 5.6: The measured suction time for a static drop, $t_{\mathcal{G}}$, as a function of the scale $\mu V_0/\delta^2\sigma$, defined in eq (5.5).

In Figure 5.6 the values for the capture time $t_{\mathcal{G}}$ for a static drop are plotted as a function of the term $\mu V_0/\delta^2\sigma$, determined in Eq. (5.5). The linear dependence of these values serves as an experimental confirmation of the scaling expressed by Eq. (5.5). The best fit of the experimental data

yields for this particular wall wettability

$$t_{\mathcal{G}} \approx 1036.0 \frac{\mu V_0}{\delta^2 \sigma}. \tag{5.6}$$

5.3 Interaction of an aerodynamically driven drop with a single groove

To better understand and model the mechanisms leading to the possible drop passing over the groove or drop pinning/sucking by the groove, the scalings and models introduced in Section 4.3 need to be considered.

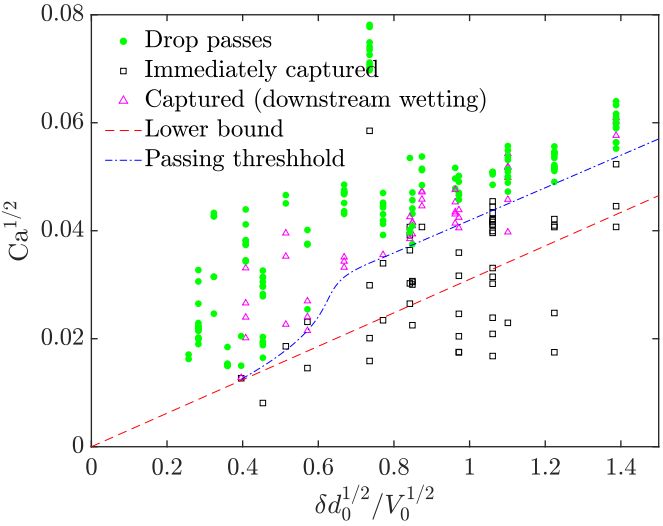

Figure 5.7: A nomogram of the major outcomes of the drop interaction with the groove for different capillary numbers, drop and groove sizes, presented in dimensionless form. The lower bound curve to the theoretical estimation (5.7). Dash-dotted line represents the empirically determined boundary for a drop to pass a groove.

These length scales are only correct for drops with very small Bond numbers which move with a very small velocity, corresponding to small capillary numbers. Moreover, these expressions can be used also for the creation a relevant dimensionless parameters for the descriptions of the hydrodynamic

phenomena at higher drop velocities, higher drop deformations and higher Bond numbers.

One of the important parameters influencing the outcome of the interaction with a groove of a moving drop is the ratio of the typical time of the drop passing over the groove, $t_{\mathrm{drop}} \sim d_0/v$ and the typical time $t_{\mathcal{G}}$ required for the suction of the entire drop volume. It is obvious that drop passing is not possible if $t_{\mathcal{G}} < t_{\mathrm{drop}}$. The lower bound for the drop passing is determined from the comparison of these two characteristic times with the help of Eq. (5.5) as

$$\mathrm{Ca}^{1/2} \approx 0.031 \frac{\delta d_0^{1/2}}{V_0^{1/2}}. \tag{5.7}$$

In Figure 5.7 various outcomes of the interactions of a single drop with a groove are shown for various capillary numbers, drop volumes and groove thicknesses. The outcomes are grouped in three major regimes: drop passes the groove, is immediately captured or captured after downstream wetting. On the nomogram in Figure 5.7 also a straight line corresponding to the predicted lower bound for drop passing, determined in (5.7), is plotted. It is remarkable that the predicted lower bound is indeed rather close to the threshold conditions for drop passing. Some underestimation can be explained by the drop deformation by the aerodynamic forces. Therefore, the drop length is in fact larger than d_0, estimated from the static drop situation.

The scaling shown in Figure 5.7 allows determination of the boundaries for the conditions corresponding the drop immediate capture. However, it is not able to distinguish the regimes of drop passing and drop capture after wetting of the rear side of the groove. This means that the physics of the drop capture involves further forces.

Some of the observed drops have been captured by the groove even though their velocity exceeded the threshold. Such cases are marked by the magenta triangles in Figure 5.7. They correspond to drops being captured after the rear side of the groove was wetted, as in the example in Figure 5.2c. At some experimental conditions for the same set of the experimental parameters different outcomes, passing or capturing, are observed with a certain probability. Nevertheless, the experiments show that these outcomes are influenced also by the gravity and the inertial terms of the liquid in the drop.

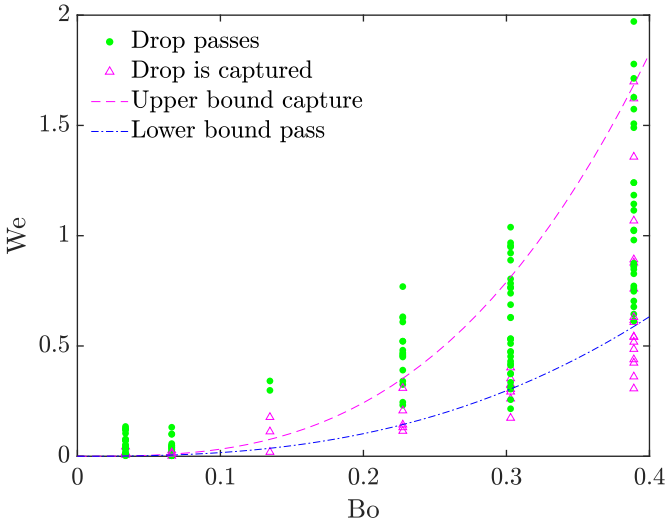

Figure 5.8: A nomogram of the two major drop outcomes for different Weber and Bond numbers. The dashed line correspond to the upper bound for the drop capture and the dash-dotted line to the lower bound for the drop passing. Cases of immediate capture are not shown on this nomogram. Their appearance window is determined in Figure 5.7.

The ratio of the inertial terms in the drop and the capillary pressure associated with the groove width is related by the Weber number (Eq. 2.3) defined as

$$\mathrm{We} = \frac{\varrho v^2 \delta}{\sigma}. \tag{5.8}$$

At higher Weber numbers the pressure over the groove entrance is lower due to the fast drop motion and reduced suction speed. Moreover, one can imagine that at some high enough drop velocities it can simply jump over the groove with only minor suction.

The suction rate in the groove is influenced also by gravity. This effect is governed by the Bond number (Eq. 2.4) defined as

$$\mathrm{Bo} = \frac{\varrho g \delta^2}{\sigma}. \tag{5.9}$$

In Figure 5.8 a nomogram of the outcome after the drop-groove interactions are shown for various Weber and Bond numbers. Only the cases of capture are considered when it occurs after the wetting of the rear side of the groove. The cases of immediate capture are not shown, since their operational window is already determined in Figure 5.7.

The two lines in Figure 5.8 correspond to two empirically observed thresholds. One is the upper bound for the drop capture and the second is the lower bound for the drop passing. Between these two bounds both outcomes are observed with a certain probability. It is obvious that for higher Bond numbers the minimum threshold Weber number at which the drop still passes the groove, increases. For Weber numbers below the upper bound for capture, the probability for capture also increases with the Bond number.

6 Aerodynamically driven rivulets

This chapter presents observations of shear driven rivulets and their formation. Different effects have been characterized and offer a basis for further investigations. Only very few studies on shear driven rivulets have been published. Most investigations concerning rivulets consider gravity as the sole driving force. They are briefly summarized in order to place the characterizations of this study into context. Next, the mechanism used to create a steady water volume flow is introduced. Then the experimental procedure is explained and typical observations are characterized. Finally, regime maps compiling the observed behaviors on four different surfaces at varying air and water flow rates are presented.

Some of the data was gathered during the Bachelor thesis by Wickersheim (2019).

6.1 Literature overview

Rivulets only form under certain conditions. Foremost, the liquid must only partially wet the substrate. If this condition is met, rivulets can have three different origins: the tail of a moving drop, the constriction of a thin film, or a steady stream of liquid. Forming a rivulet requires a driving force. The typical driving forces are gravity on an inclined plate, an aerodynamic force, or a combination of both. Besides exterior water management of vehicles, understanding rivulet motion is essential for many processes, e.g. trickle bed reactors, structured packings, runback ice accretion on aircraft or river sediment transport (Herrada et al., 2015).

In recent years, Marshall and Ettema (2004) worked on shear driven rivulets. Their work was motivated by understanding rivulet flow over a range of gravity situations. Experiments were performed between 0 g and 1 g. The investigated rivulet behavior is relevant for aircraft on sharply curved

trajectories as well as space flight. These researchers list future Lunar and Martian space stations as benefactors of their research.

Rivulet descriptions as well as modeling approaches are introduced in reference to experiments with a steady liquid stream on an inclined substrate. Through observations and experiments Culkin and Davis (1984), Nakagawa and Scott (1984), and Le Grand-Piteira et al. (2006) characterized rivulets. The introduced regimes primarily depend on wetting properties of the substrate, volumetric flow rate Q of the liquid as well as the tilting angle β of the substrate.

The five regimes are:

1. Stream of drops ($Q < Q_{\mathrm{r}}$)
   Not enough volume of liquid is fed into the rivulet. A chain of individual drops moving in the same direction is the result.

2. Rivulet - straight ($Q_{\mathrm{r}} \leq Q < Q_{\mathrm{m}}$)
   Sufficient liquid volume is fed into the rivulet, the path the rivulet follows is determined by the steepest incline of the substrate.

3. Rivulet - meandering ($Q_{\mathrm{m}} \leq Q < Q_{\mathrm{m,d}}$)
   Meandering of rivulets sets in after a critical volumetric flux Q_{m} is reached. Instabilities lead to a deviation from the straight path. These instabilities may be caused by surface heterogeneities, fluctuations in liquid flux due to noise at the injector, or motion of the gaseous phase.

4. Rivulet - dynamically meandering ($Q_{\mathrm{m,d}} \leq Q < Q_{\mathrm{m,rs}}$)
   Similar to the third regime, steady meandering, perturbations result in a deviation in the rivulet path. A second critical volumetric flux $Q_{\mathrm{m,d}}$ is found with the difference that the rivulet does not settle to a stationary path. (Le Grand-Piteira et al., 2006)

5. Rivulet - restable regime ($Q_{\mathrm{m,rs}} < Q$)
   By maintaining an exact constant volume flux $Q > Q_{\mathrm{m}}$ meandering can be suppressed. As a result, a braided structure forms. Mertens et al. (2005) explain this pattern by the interaction between surface tension and fluid inertial forces.

6.1.1 Straight rivulets

This section focuses on the second rivulet regime, straight rivulets. Towell and Rothfeld (1966) were among the first to systematically describe rivulets. They introduced two models describing the geometry of straight rivulets. Each of the models is based on one of two limiting assumptions: either the cross-sectional geometry of a rivulet is assumed to be a sector of a circle, or the rivulet is assumed to be wide and flat.

The geometry assumption of a circular sector was further considered by Schmuki and Laso (1990) and Hoffmann (2010). It is limited to small rivulets where surface tension is the dominating force influencing the cross-sectional shape.

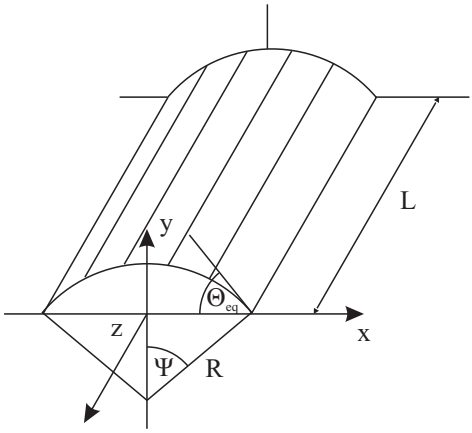

Figure 6.1: Schematic of a circular section rivulet geometry (adapted from Schmuki and Laso (1990))

Figure 6.1 shows the geometry of a rivulet with an assumed sector of circular cross-section, where L represents the length of the rivulet, Ψ the polar subtended angle and $\Theta_{\text{eq.}}$ the equilibrium contact angle introduced in Section 2.2.1.

Schmuki and Laso (1990) estimated the rivulet height

$$\delta(x) = R(\cos\Psi - \cos\Theta_{\text{eq.}}), \tag{6.1}$$

as well as the width of the rivulet

$$w = 2R \sin \Psi. \tag{6.2}$$

Using this simplification as well as the Navier-Stokes and Young-Laplace equations, it is possible to calculate the Laplace pressure for the rivulet

$$\Delta P = -\frac{\sigma \delta''(y)}{(1 + \delta'^2(y))^{3/2}}, \tag{6.3}$$

where $\delta' = \partial\delta/\partial x$ and $\delta'' = \partial^2\delta/\partial x^2$. Hoffmann (2010) introduced further simplifications resulting in the geometry of the rivulet not depending on the contact angle of the liquid substrate combination; only the tilting angle of the plate, viscosity and volumetric flow rate Q influence the size of the rivulet.

The second model introduced by Towell and Rothfeld (1966) was developed in order to describe volumetric flow rates of the liquid where the effect of gravity can no longer be neglected. They assumed $R \gg \delta$ and $R > \kappa$ on hydrophilic substrates with small contact angles, κ being the capillary length. For these cases the correlation

$$\frac{\mu Q \cot \alpha}{w\sigma} \sqrt{\frac{\varrho g \cos \alpha}{\sigma}} = \frac{8}{3} \left(\sin \frac{\Theta}{2} \right)^3 \tag{6.4}$$

was introduced.

Determining the volumetric flux of a rivulet is of great importance. It is possible to calculate said flux, knowing the geometry of a rivulet, as shown by Towell and Rothfeld (1966):

$$Q = \int_{-\frac{l}{2}}^{\frac{l}{2}} \int_{0}^{\delta} u(x, y) \, \mathrm{d}y \, \mathrm{d}x \tag{6.5}$$

Duffy and Moffatt (1995) used a different approach to describe a straight rivulet. They introduced a Bond number

$$\mathrm{Bo}_r = \frac{w}{2} \sqrt{\frac{\varrho g |\cos \beta|}{\sigma}} \tag{6.6}$$

from which the rivulet height δ can be estimated:

$$\delta(x) = \tan\Theta_{\mathrm{eq}} \sqrt{\frac{\sigma}{\varrho g |\cos\alpha|}} \left[\frac{\cosh \mathrm{Bo}_r - \cosh\left(\mathrm{Bo}_r \frac{x}{w/2}\right)}{\sin \mathrm{Bo}_r} \right]. \tag{6.7}$$

This equation is valid for a Newtonian fluid of constant density and viscosity having a steady volume flow rate for an inclination of the plate $0 < \beta < 90°$.

6.1.2 Meandering rivulets

An increase in the volume flux Q results in a curvature of the rivulet. Culkin and Davis (1984) as well as Couvreur and Daerr (2012) investigated meandering in rivulets. They found that the path of the rivulets is mainly influenced by inertial forces occurring due to contact line instabilities. The distinction between rivulet regime three and four, static and dynamic meandering, is explained by pinning forces. In static meandering a stationary state is reached.

Figure 6.2a shows the experimental setup used by Le Grand-Piteira et al. (2006) in order to investigate rivulets is shown. The inclination β of the substrate can be altered in order to increase or decrease the influence of the gravitational force. A stationary meandering case, the third regime, is depicted. Figure 6.2b shows a cross-sectional cut of the meandering rivulet with the corresponding geometric parameters, contact angles and acting forces.

Precisely describing the path taken by a rivulet is still a challenging task. Even rivulets with a straight trajectory exhibit small distortions of the contact lines that are small compared to the width of the rivulet. Increasing the volume flux $Q > Q_{\mathrm{m}}$ results in dynamic alterations of the trajectory, which stabilize after a finite time. However, it may take multiple hours for this meandering to stabilize. (Couvreur and Daerr, 2012)

A hysteresis in the path can be observed upon reducing the volumetric flux below Q_{m}. After a stationary meandering state sets in, the rivulet retains the meandering path due to pinning forces. (Culkin and Davis, 1984)

It is possible to calculate the critical volumetric flux Q_{m}, as shown by Couvreur and Daerr (2012). The calculation relies on the centrifugal forces in reference to the geometry of the rivulet. Fathi et al. (2014) disproved the calculations by Couvreur and Daerr (2012), yet did not offer an alternative

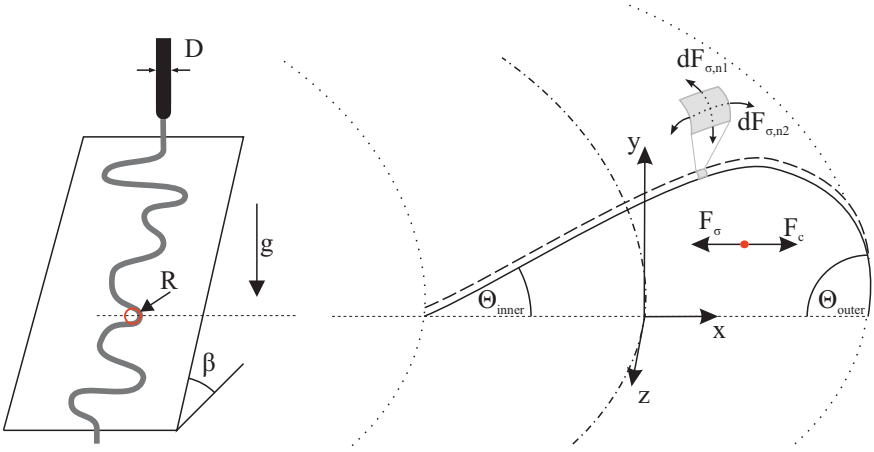

(a) Sketch of the experimental setup used by Le Grand-Piteira et al. (2006) to investigate gravity driven rivulets.

(b) Sketch of a meandering rivulet cross section. Acting inertial force F_c and surface tension force F_σ are shown. The force balance results in the asymmetry of the rivulet.

Figure 6.2: Experiment and geometry definition of rivulet experiments (adapted from Rettenmaier (2019))

solution. For further information on these calculations, the reader is referred to the cited literature.

6.2 Pumping mechanism

A rivulet requires a constant liquid volume flow being pumped onto the substrate. In the present experiments this volume flow is generated by a precision gear pump which is regulated and monitored by a Coriolis mass flow meter. A Flusys WADose Lite Gear pump consisting of two components has been used. A magnetic actuator generating a rotating magnetic field and an interchangeable gear head. When the pump and actuator operate within their specified parameters an oscillation free volume flow is generated.

A hydraulic diagram of the pumping mechanism is shown in Figure 6.3. A tube connects the water reservoir with the gear head. From the head another

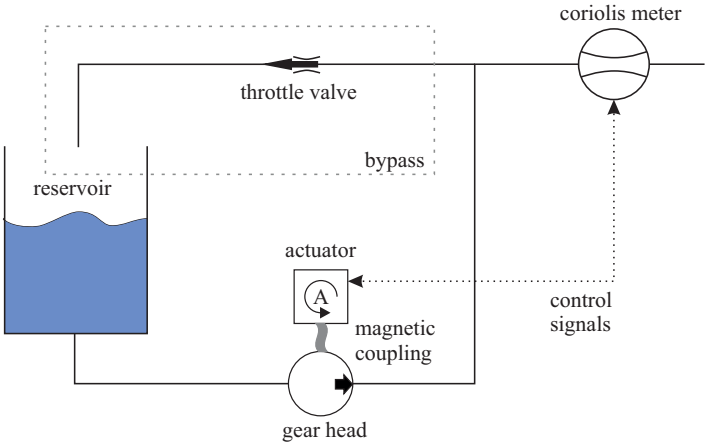

Figure 6.3: Hydraulic diagram of the pumping mechanism.

pipe leads to a crossing where the liquid flow is split into two directions. A bypass leads a portion of the flow back to the reservoir, while the main flow is directed through a Coriolis mass flow meter. The meter and actuator are connected by a serial bus. The control unit of the actuator constantly receives the current mass flux. A user interface allows setting the desired mass or volume flow rate at the control unit.

In order to generate an oscillation free volume flowrate, the gear head needs to operate within its design parameters. Generating volumes flows as low as $Q = 1\ {}^{\mathrm{ml}}/_{\mathrm{min}} = 1.67 \times 10^{-8}\ {}^{\mathrm{m}^3}/_{\mathrm{s}}$ thus requires the bypass. A throttle valve regulates the amount of liquid returned to the reservoir by the bypass.

The liquid is pumped onto the substrate through a 1 mm bore hole. This bore hole and the pumping mechanism are connected by silicone tubing. The elasticity of the silicone tubing acts as an additional dampener for potential oscillations in the flow rate.

6.3 Experimental procedure

Considering the literature on rivulets the experimental procedure is of great importance to their behavior. For this reason it is summarized in this section.

In this study purified water is used for all measurement. The water is purified using an osmosis filter. The same four substrates as for the single drop motion experiments (Section 4.2) have been used while investigating rivulets. In Table 6.1 the wetting properties of the substrates are listed.

Table 6.1: Wetting properties for the surfaces used in the rivulet experiments: advancing Θ_{adv} and receding Θ_{rec} contact angles and the hysteresis $\Delta\Theta = \Theta_{adv} - \Theta_{rec}$.

Surface	Θ_{adv}	Θ_{rec}	$\Delta\Theta$
Aluminum	93°	33°	60°
Varnished aluminum	73°	36°	37°
Polymethyl methacrylate	71°	46°	25°
Varnished steel	90°	30°	60°

Each set of experiments began by setting the desired gas flow velocity in the wind tunnel. If a constant value has been reached the liquid volume flow was increased to the target value. After the parameters for the measurement point have been reached the system was allowed 60 s to settle.

Table 6.2: Investigated $\mathrm{Re}_{\mathcal{H}}$ ranges with corresponding increments.

$\mathrm{Re}_{\mathcal{H}}$	increment $\Delta\mathrm{Re}_{\mathcal{H}}$
5×10^3 - 10×10^3	1×10^3
10×10^3 - 30×10^3	2×10^3

The behavior was characterized for the gas flow velocities listed in Table 6.2. Liquid volume flow rates from $Q = 1$ $^{\mathrm{ml}}/_{\mathrm{min}} = 1.67 \times 10^{-8}$ $^{\mathrm{m}^3}/_{\mathrm{s}}$ to $Q = 40$ $^{\mathrm{ml}}/_{\mathrm{min}} = 6.67 \times 10^{-7}$ $^{\mathrm{m}^3}/_{\mathrm{s}}$ in increments of $\Delta Q = 1$ $^{\mathrm{ml}}/_{\mathrm{min}} = 1.67 \times 10^{-8}$ $^{\mathrm{m}^3}/_{\mathrm{s}}$ have been investigated. For each wind tunnel velocity the behavior of each liquid flow rates has been surveyed. The minimal as well as maximal values shown here were a result of preliminary investigations. For Reynolds numbers lower than $\mathrm{Re}_{\mathcal{H}} < 5 \times 10^3$ the aerodynamic forces did not suffice to move the liquid downstream on the substrate. The highest investigated Reynolds number $\mathrm{Re}_{\mathcal{H}} = 30 \times 10^3$ corresponds to the highest one attainable at any ambient condition. The lower limit of the liquid volume

flow rate is determined by the operating parameters of the pumping mechanism. At such small flow rates the full capacity of the bypass is used. In contrast, at high liquid volume flow rates the pressure required to pump the liquid through the bore in the surface results in a water fountain at the bore. The combination of such a fountain and a gas flow results in the liquid being sprayed onto the ceiling and side walls, making observations impossible. Images for both limiting cases are shown in Section 6.4.

For each gas flow velocity and liquid volume flux the behavior has been observed. Using this data a regime map for each surface has been compiled. In each of the seven regimes images have been recorded at 30 fps using two iDS cameras (Section 3.3). Both cameras were located next to each other, looking perpendicularly through the ceiling onto the substrate surface. During post processing both images were stitched together. Using two cameras allowed a high spatial resolution of the substrate, while its whole length was within the field of view.

6.4 Observations

Seven regimes have been defined while investigating rivulets on the four different substrates. Each regime is assigned a symbol that is introduced in this section while highlighting its characteristic properties.

The black patch visible on all images is a cover for the pipette opening using in other experiments.

Not characterizable ($\times$)

While explaining the experimental procedure lower and upper limits have been introduced. Two examples of these limits are given here. First, the lower limit, where the aerodynamic forces do not suffice for a rivulet to form. Second, the upper limit where a fountain at the bore results in a spray contaminating wind tunnel ceiling and walls.

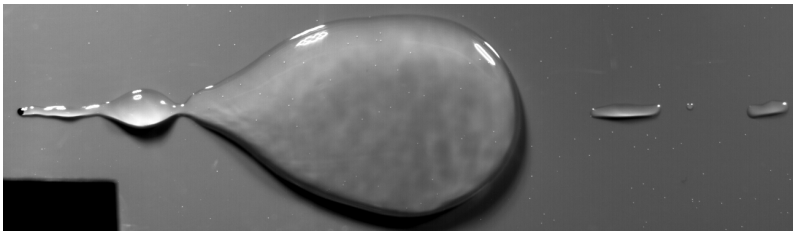

Figure 6.4: Stitched top view image of the behavior at the lower limit of the parameter space.
Surface: varnished aluminum ($\Theta_{\mathrm{adv,\ cr}} = 73°;\ \Theta_{\mathrm{rec,\ cr}} = 36°$)
Flow parameters: $Q = 1\ {}^{\mathrm{ml}}/_{\mathrm{min}}$, $\mathrm{Re}_{\mathcal{H}} = 5 \times 10^3$

In Figure 6.4 an image of the lower limit of the parameter space is shown. Due to the low flow velocity in the channel the aerodynamic forces do not suffice to constantly move the liquid downstream. As a result the liquid accumulates until its cross-sectional area perpendicular to the flow is sufficiently large for the aerodynamic force to move it downstream.

Another parameter configuration that cannot be categorized is shown in Figure 6.5. The pressure required to pump the liquid volume flow rate of $Q = 40\ {}^{\mathrm{ml}}/_{\mathrm{min}}$ through the bore results in a fountain at the bore. It is immediately torn apart by the gas flow. As a consequence, drops are sprayed onto all test section surfaces, blocking the view of the rivulet on the substrate.

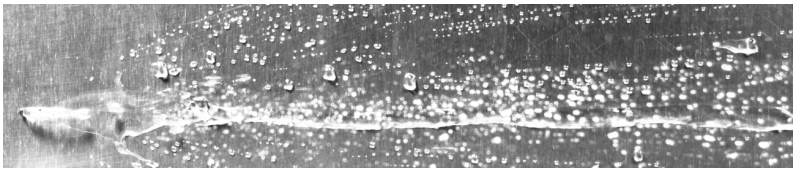

Figure 6.5: Stitched top view image of the behavior at the upper limit of the parameter space.
Surface: aluminum ($\Theta_{\mathrm{adv,\ cr}} = 93°;\ \Theta_{\mathrm{rec,\ cr}} = 33°$)
Flow parameters: $Q = 40\ {}^{\mathrm{ml}}/_{\mathrm{min}}$, $\mathrm{Re}_{\mathcal{H}} = 10 \times 10^3$

Straight rivulet (□)

In Figure 6.6 an image of a straight rivulet on the aluminum substrate sample is shown. The small deviations from a straight path can be explained by minute heterogeneities of the substrate. Since the deviations in trajectory

are smaller than the width of the rivulet, this is not classified as meandering.

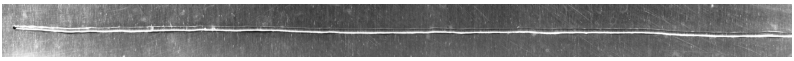

Figure 6.6: Stitched top view image of a straight rivulet.
Surface: aluminum ($\Theta_{\text{adv, cr}} = 93°$; $\Theta_{\text{rec, cr}} = 33°$)
Flow parameters: $Q = 10\ ^{\text{ml}}/_{\text{min}}$, $\text{Re}_{\mathcal{H}} = 10 \times 10^3$

Meandering rivulet (▽)

The sequence of images shown in Figure 6.7 highlights how a rivulet meanders on a varnished aluminum substrate. The bends and turns of the rivulet change over time. Steady meandering in a turbulent channel flow means that bends and turns of similar size move in streamwise direction over time, similar to dynamically meandering rivulets on inclined surfaces.

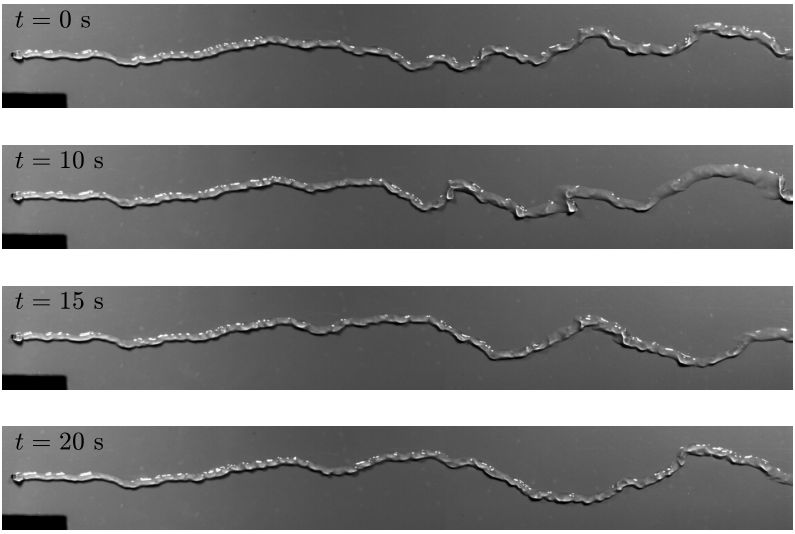

Figure 6.7: Sequence of stitched top view images showing a meandering rivulet.
Surface: varnished aluminum ($\Theta_{\text{adv, cr}} = 73°$; $\Theta_{\text{rec, cr}} = 36°$)
Flow parameters: $Q = 15\ ^{\text{ml}}/_{\text{min}}$, $\text{Re}_{\mathcal{H}} = 16 \times 10^3$

Drop chain (•)

Chains of drops were only observed on Polymethyl methacrylate (PMMA). In Figure 6.8 such a drop chain is shown. The scratches and defects visible on the image are located on the outside and do not influence the experiment. They are a remnant of machining. Drop chains mainly occurred for low liquid flow rates $Q < 13$ $^{\mathrm{ml}}/_{\mathrm{min}}$. PMMA was the substrate with the highest critical receding contact angle that has been investigated. Therefore individual drops are less likely to form a tail while moving, inhibiting rivulet formation.

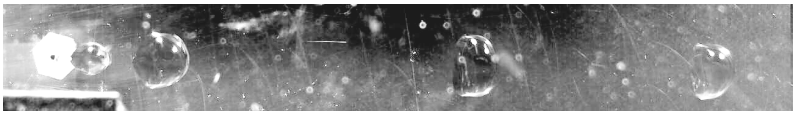

Figure 6.8: Top view image of a drop chain. Visible scratches are located on the outer wall side and do not influence wetting and the experiments.
Surface: PMMA ($\Theta_{\mathrm{adv,\ cr}} = 71°$; $\Theta_{\mathrm{rec,\ cr}} = 46°$)
Flow parameters: $Q = 5$ $^{\mathrm{ml}}/_{\mathrm{min}}$, $\mathrm{Re}_{\mathcal{H}} = 10 \times 10^3$

Surging rivulet (◇)

In Figure 6.9 four images of an surging rivulet are shown. A surging rivulet follows a straight path in downstream direction and its motion is mainly governed by the aerodynamic forces. This is underlined by the fact that they are only observed at higher channel flow velocities, $\mathrm{Re}_{\mathcal{H}} > 20 \times 10^3$. The surges, local changes in the rivulets cross section area, travel downstream with the rivulet. In the image sequence some of the surges have been highlighted indicating that they occur periodically.

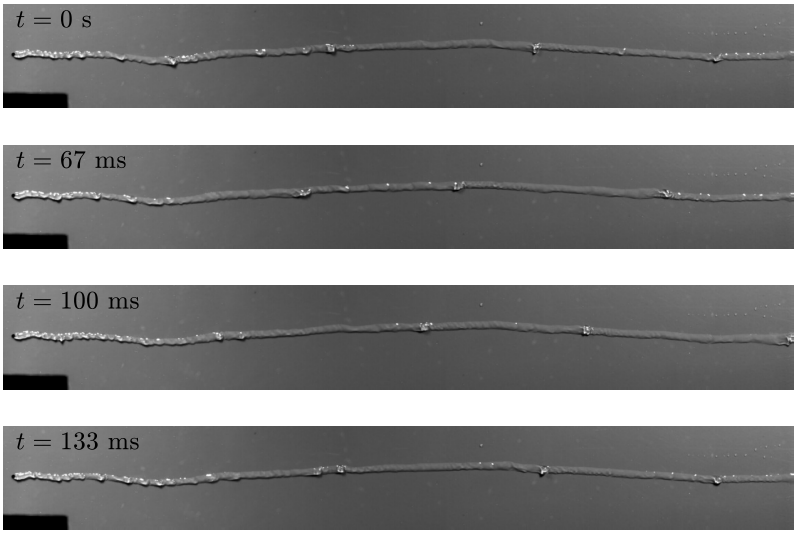

Figure 6.9: Sequence of stitched top view image of an surging rivulet.
Surface: varnished aluminum ($\Theta_{\text{adv, cr}} = 73°$; $\Theta_{\text{rec, cr}} = 36°$)
Flow parameters: $Q = 15\ ^{\text{ml}}/_{\text{min}}$, $\text{Re}_{\mathcal{H}} = 26 \times 10^3$

Drop shedding (◯)

Drop shedding is strongly connected to the surging behavior of a rivulet. The increase in cross-sectional area results in a greater area of attack for the gas flow. If the attacking force at an accumulation exceeds the surface force, one or multiple drops are ripped from the rivulet. These drops follow the downstream direction of the gas flow. Because drop shedding only occurs at surging rivulets the same marker color has been chosen.

Figure 6.10: Stitched top view image of a rivulet shedding drops.
Surface: varnished aluminum ($\Theta_{\text{adv, cr}} = 73°$; $\Theta_{\text{rec, cr}} = 36°$)
Flow parameters: $Q = 24\ ^{\text{ml}}/_{\text{min}}$, $\text{Re}_{\mathcal{H}} = 30 \times 10^3$

An image of an surging rivulet where drops are shed is shown in Figure 6.10. Two downstream traveling drops that have been ripped from the rivulet have been highlighted.

Strong drop shedding (△)

As the name of this regime indicates, it is closely related to the drop shedding regime. Due to the high frequency with which drops are being ripped from the rivulet a separate regime has been introduced. This behavior is only present for the highest gas and liquid flow rates. In Figure 6.11 an image typical for this regime is shown.

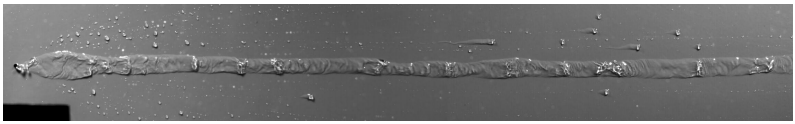

Figure 6.11: Stitched top view image of a rivulet with strong drop shedding.
Surface: varnished aluminum ($\Theta_{\text{adv, cr}} = 73°$; $\Theta_{\text{rec, cr}} = 36°$)
Flow parameters: $Q = 38\ ^{\text{ml}}/_{\text{min}}$, $\text{Re}_{\mathcal{H}} = 30 \times 10^3$

Rivulet breakup (∗)

Experiments for which a rivulet disintegrated after a discrete distance have been assigned to the breakup regime. Three different types of rivulet breakup have been observed: drop, bead and film breakup.

Generally, rivulet breakup has been observed for low gas flow velocities, $\text{Re}_{\mathcal{H}} \leq 10 \times 10^3$. The shear forces required to contain the liquid flow within the boundaries of a rivulet are not present.

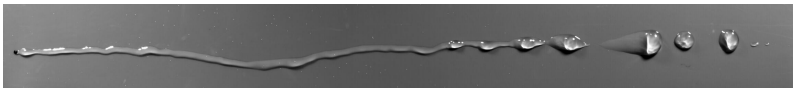

Figure 6.12: Stitched top view image of a rivulet breaking up in individual drops.
Surface: varnished steel ($\Theta_{\text{adv, cr}} = 90°$; $\Theta_{\text{rec, cr}} = 30°$)
Flow parameters: $Q = 5\ ^{\text{ml}}/_{\text{min}}$, $\text{Re}_{\mathcal{H}} = 10 \times 10^3$

The first type of rivulet breakup is shown in Figure 6.12. The rivulet formed directly behind the bore widens into beads. These beads separate from the rivulet into drops after reaching a distinct liquid volume. The drops then move individually in streamwise direction.

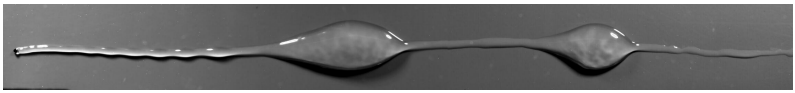

Figure 6.13: Stitched top view image of a rivulet breaking up by forming beads.
Surface: varnished aluminum ($\Theta_{\text{adv, cr}} = 73°$; $\Theta_{\text{rec, cr}} = 36°$)
Flow parameters: $Q = 15$ $^{\text{ml}}/_{\text{min}}$, $\text{Re}_{\mathcal{H}} = 6 \times 10^3$

The second type of rivulet breakup is similar to the first. It occurs at three time larger liquid flow rates and half size Reynolds numbers. Again beads are formed that increase in size and travel along the rivulet in downstream direction. An image of this behavior is shown in Figure 6.13

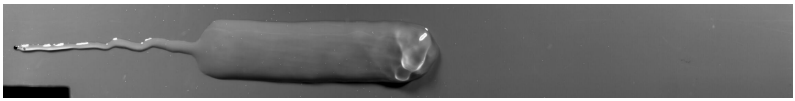

Figure 6.14: Stitched top view image of a rivulet breaking up by forming a film.
Surface: varnished steel ($\Theta_{\text{adv, cr}} = 90°$; $\Theta_{\text{rec, cr}} = 30°$)
Flow parameters: $Q = 5$ $^{\text{ml}}/_{\text{min}}$, $\text{Re}_{\mathcal{H}} = 5 \times 10^3$

In Figure 6.14 an experiment where a rivulet transitioned into a film and moved downstream is shown. Because the rivulet ended with this transition and the balance of forces being different for shear driven films the rare cases where they formed have been classified as rivulet breakup.

6.5 Regime maps

In Figure 6.15 the regime maps for all four investigates substrates are shown. The liquid volume flow rate Q is plotted on the abscissas and the channel Reynolds number $\text{Re}_{\mathcal{H}}$ on the ordinates. The axis of the four plots are identical, allowing to compare the effect the wetting properties has on the rivulet behavior. Each of the eight previously introduced characteristic behaviors are represented by an individual symbol.

For all black symbols ($\times$, $\bullet$, $*$) no rivulet formed. At high liquid volume flow rates $Q \gtrapprox 35$ $^{\text{ml}}/_{\text{min}}$ a fountain formed at the bore limiting the observations. For $\text{Re}_{\mathcal{H}} \lessapprox 8 \times 10^3$ and $Q \lessapprox 22$ $^{\text{ml}}/_{\text{min}}$ no stable rivulet over the substrate formed. Since rivulets formed on all substrates at these low gas flow rates and liquid flow rates between 22 $^{\text{ml}}/_{\text{min}} \lessapprox Q \lessapprox 32$ $^{\text{ml}}/_{\text{min}}$ can be

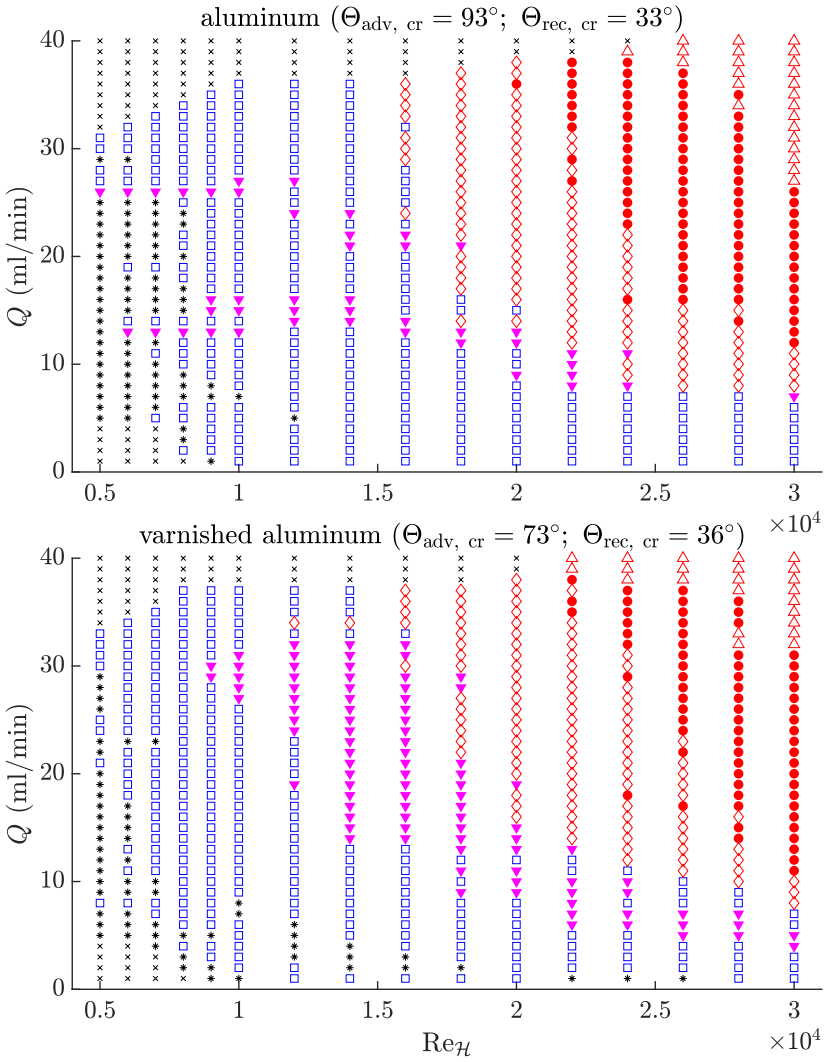

Figure 6.15: Regime maps of all investigated substrates. Symbols: (×) not characterizable, (□) straight rivulet, (▽) meandering rivulet, (•) drop chain, (◇) surging rivulet, (◯) drop shedding, (△) strong drop shedding, (∗) rivulet breakup

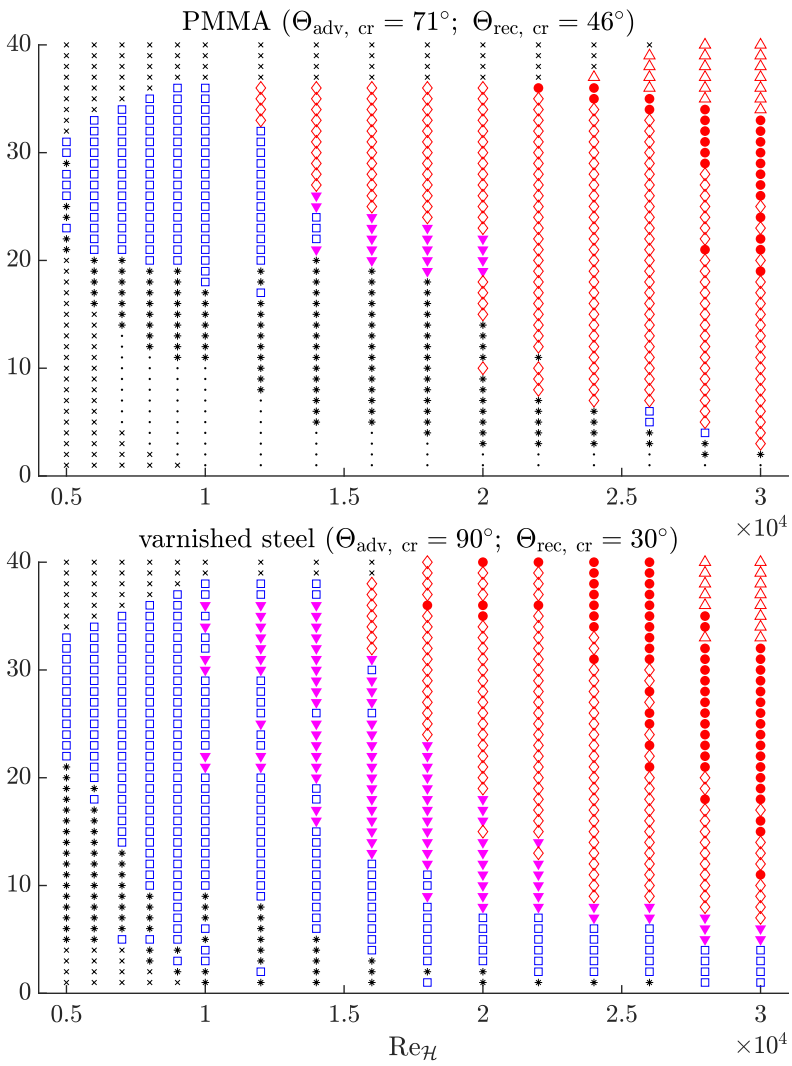

explained by the greater cross-sectional area of the rivulets. The increase in area leads to a higher rivulet resulting to it being exposed to higher shear forces that stabilize it.

The only substrate for which a chain of individual drops formed was PMMA. It having the highest critical receding contact angle explains this behavior. The liquid is less likely to form long tails which merge into a rivulet as it occurs on all other substrates.

As for the straight (□) and meandering (▽) the difference between aluminum and varnishes steel is noteworthy. Both substrates have similar critical contact angles, yet their behavior differs significantly. On aluminum it is less likely that a rivulet forms for $\mathrm{Re}_{\mathcal{H}} \lessapprox 8 \times 10^3$. Furthermore, on aluminum rivulets are less likely to meander. These dissimilarities in behavior indicates that further factors need to be accounted for when investigating rivulets.

On all substrates a similar surging regime (◯, ◇, △) has been found. Since it is located on each upper right quadrant of the diagrams the aerodynamic forces play a greater role than the substrate wettability. Wettability though influences the likelihood with which drops are ripped from the rivulet. PMMA having the higher critical receding contact angle forms a surging rivulet less likely to shed drops.

7 Conclusion and Outlook

The physics behind aerodynamically driven wall-bounded liquid motion have not yet been fully understood. Furthermore, publications on observations or models that allow prediction of the behavior of such multiphase flows are scarce. Consequently, the present study sets out to contribute to this field, by investigating the smallest amount of aerodynamically moved liquid: single drops.

Several experiments with drops of various volumes on real world substrates with different wetting properties have been investigated. These investigations resulted in a theoretical, physics based model as well as a reasonable scaling of the problem. The dimensionless attack velocity that relates the wetting properties of the liquid/solid combination to the local gas flow velocity proved appropriate. This model allows prediction of whether a drop moves over a surface due to aerodynamic forces, as well as its velocity if it does. The good agreement between the model and experimental observations highlights the importance of the local gas flow velocity, an insight first introduced in this research.

While observing the motion of single drops, a detailed investigation of the critical contact angle was conducted. Drops moving with a constant mean velocity in a stick-slip motion were studied using a cross-correlation between the velocity and the contact angle. This showed that the best correlation between both is found using a significantly higher threshold value of the advancing contact angle as measured using a quasi-stationary method. Furthermore, it was shown that numerical simulations using this increased critical contact angle as a boundary condition resulted in excellent agreement between experiment and simulation. Both, the results of the cross-correlation and the the physics based numerical simulation, then raise the question whether there is a necessity to introduce a dynamic critical contact angle?

Using the model predicting individual drop motion, the interaction between a moving drop and a single groove was investigated. Since grooves play an essential role for applications involving wall-bounded liquid motion, a substrate with a generic groove of variable width and 90° edge angles was selected for this experimental campaign. Three distinct outcomes of the experiments were observed. Using the previously introduced scaling, capillary forces in the groove, the influence of drop inertia as well as gravity acting on the drop while in transit over the groove monograms with clear boundaries separating each outcome were introduced. By doing so it is now possible to predict whether a drop is captured by a groove or if the majority of its volume continues a downstream motion after passing the groove. In addition, the observations provided new insight into the interaction between drops and grooves. For a drop to pass a groove a liquid bridge spanning both sides of the groove is necessary.

The third part of this study focuses on rivulets and the conditions under which they form as well as their behavior. The observations on different substrates allowed compiling regime maps. Since this work presents one of the first studies on aerodynamically driven rivulet formation, these regime maps offer new insights. The importance of the critical capillary number became apparent in the polymethyl methacrylate experiments. This critical capillary number is twice as high as for the other investigated substrates, significantly restricting the condition under which a rivulet is formed. Besides this, a regime mainly governed by aerodynamic forces was delimited.

Lastly, an additional benefit of the presented research is its value for other researchers. The collected experimental data can be used to validate numerical prediction tools. One example for such a validation was shown with the comparison of the single drop motion measurements and simulations.

Outlook

In addition to the models and scalings introduced, this study provides a foundation for future research. A first step could be to verify and/or extend models to other substrate/liquid combinations. Either more hydrophobic surfaces, water/glycerol mixtures or water with surfactants would be of interest. Discussions with industrial partners indicated an interest in the

behavior of drops at the intersection between two substrates with different wetting properties. Furthermore, understanding the conditions under which drops breakup is relevant for many application.

As for the single groove investigations, a study of other geometries, i.e. rounded or phased edges as well as different groove depths, would be possible. Changing the wetting properties of the surface or within the groove also holds great potential for further studies.

The possibility to experiment with rivulets allows unexplored ares of multiphase flows to be systematically studied. Important goals would be: measuring the flow velocity of the rivulet using particle tracking velocimetry, introducing an appropriate scaling and investigating the surging regime.

All the suggested investigations are possible without major modifications to the wind tunnel. Also the question of gravitational influences has been discussed throughout the work. This could be achieved by rotating the wind tunnel around its streamwise axis. By doing so the combination of gravitational and aerodynamic forces on the liquid could be investigated.

Nomenclature

Small Greek Characters

β	$^\circ$	surface inclination angle
$\delta(x)$	m	rivulet height
δ	m	groove distance
ϵ_Θ	$^\circ$	contact angle binarization threshold value
ϵ_v	$^{\mathrm{m}}/_{\mathrm{s}}$	contact line velocity binarization threshold value
κ	$-$	characteristic liquid film curvature
κ_{eq}	Hz	characteristic frequency
λ	m	length scale of evolution equation
λ_{MK}	m	distance between adsorption sites (MK theory)
μ	Pa s	dynamic viscosity
σ	$^{\mathrm{N}}/_{\mathrm{m}}$	surface tension
τ	s	lag-time shift of correlation
τ_{g}	$^{\mathrm{N}}/_{\mathrm{m}}$	aerodynamic shear stress
ϱ	$^{\mathrm{kg}}/_{\mathrm{m}^3}$	density
ϱ_{g}	$^{\mathrm{kg}}/_{\mathrm{m}^3}$	density of gas

Capital Greek Characters

Ψ	rad	polar subtended angle
Θ	$^\circ$	contact angle

Θ_δ	°	groove wall contact angle
$\Theta_{\mathrm{ac,eq}}$	°	actual, equilibrium contact angle
Θ_{app}	°	apparent contact angle
Θ_{D}	°	dynamic contact angle
Θ_{m}	°	microscopic contact angle
Θ_i	°	contact angle with $i \in$ [adv; adv,cr; rec; rec,cr; eq]

Small Roman Characters

d_0	m	drop diameter
g	$\mathrm{m/s^2}$	Earth gravitational constant
h	$\mathrm{m^2 kg/s}$	Planck constant
h_0	m	drop height
k_{B}	$\mathrm{kg\ m^2/s^2 K}$	Boltzmann constant
n	$\mathrm{1/m^2}$	number of adsorption sites per unit area
p	Pa	pressure
$p_{\mathcal{G}}$	Pa	pressure in the liquid bridge
p_∞	Pa	ambient pressure
t	s	time
$t_{\mathcal{G}}$	s	time for complete drop absorption by groove
u	m/s	velocity
u_{att}	m/s	gas flow attack velocity
u_{im}	m/s	gas flow attack velocity of incipient motion
$\tilde{u}_{\mathrm{att}}$	–	dimensionless gas flow attack velocity
$\tilde{u}_{\mathrm{im}}$	–	dimensionless gas flow incipient motion velocity

$u_{\mathcal{G}}$	$^{\mathrm{m}}/_{\mathrm{s}}$	velocity of expanding liquid bridge
v	$^{\mathrm{m}}/_{\mathrm{s}}$	drop velocity
w_{MK}	$^{\mathrm{J}}/_{\mathrm{m}}$	work per unit displacement (MK theory)
w	m	rivulet width
x	m	coordinate in streamwise direction
x_{drop}	m	drop position relative to its initial position
y	m	coordinate $\perp$ flow direction, $\parallel$ substrate
z	m	coordinate $\perp$ flow direction, $\perp$ substrate

Capital Roman Characters

A	m^2	area
A_0	m^2	projected drop area
AS	–	wind tunnel test section aspect ratio
Bo	–	Bond number
Ca	–	capillary number
$\mathrm{Ca}^\star$	–	critical dewetting capillary number
D	m	diameter
$\mathcal{D}_{\mathrm{nozzle}}$	m	inflow nozzle diameter
$\mathcal{F}$	$^{\mathrm{N}}/_{\mathrm{m}^3}$	force density per unit volume
F_i	N	force $i \in [\ \mathrm{aero}, \mu, \sigma]$
F_{c}	N	rivulet inertial force
$\Delta G_w^* t$	J	activation free energy of wetting
$\mathcal{H}$	m	wind tunnel test section height
H	–	dimensionless thickness (evolution eq.)

X	–	dimensionless coordinate (evolution eq.)
K	–	modeling coefficient
L	m	characteristic macroscopic length
L_{m}	m	microscopic length
$\mathcal{L}$	m	wind tunnel length
N_{A}	$^{1}/_{\mathrm{mol}}$	Avogadro number
ΔP	Pa	Laplace pressure in rivulet
Q	$^{\mathrm{m}^3}/_{\mathrm{s}}$	rivulet volumetric flow rate
Q_i	$^{\mathrm{m}^3}/_{\mathrm{s}}$	rivulet volumetric flow rate $i \in$ [r; m; m,d; m,rs]
R	m	radius
$R_{\mathcal{G}}$	m	liquid bridge disc radius
$R_{\Theta_{\mathrm{adv}},v_{\mathrm{adv}}}$	–	correlation value
Re	–	Reynolds number
T	–	dimensionless aerodynamic shear stress
T	K	absolute temperature (MK theory)
Tu	$^{\mathrm{m}^2}/_{\mathrm{s}^2}$	turbulence intensity
U	$^{\mathrm{m}}/_{\mathrm{s}}$	wetting velocity (MK theory)
$\bar{U}$	$^{\mathrm{m}}/_{\mathrm{s}}$	mean gas flow velocity of the test section
V	m^3	drop volume
$\mathcal{W}$	m	wind tunnel test section width
We	–	Weber number
$\mathcal{Z}$	m	coord. $\perp$ flow direction, $\perp$ substrate of test section

Indices

μ	viscous
σ	adhesion
adv	advancing
adv, cr	critical advancing
aero	aerodynamic
eq	equilibrium
m	rivulet meandering
m,d	rivulet dynamic meandering
m,rs	rivulet restable
r	rivulet formation
rec	receding
rec, cr	critical receding

Bibliography

Arjmandi-Tash, O., Kovalchuk, N. M., Trybala, A., Kuchin, I. V., and Starov, V. (2017). Kinetics of wetting and spreading of droplets over various substrates. *Langmuir*, 33(18):4367–4385, DOI: 10.1021/acs.langmuir.6b04094.

Barwari, B., Burgmann, S., and Janoske, U. (2018). Deformation and movement of adhering droplets in shear flow. In *5th International Conference on Experimental Fluid Mechanics*, Munich.

Bear, J. (1972). *Dynamics of fluids in porous media*. American Elsevier Publishing Company, ISBN: 9780444001146.

Bendat, J. S. and Piersol, A. G. (2011). *Random Data: Analysis and Measurement Procedures*, volume 729. John Wiley & Sons, Hoboken, New Jersey, USA, ISBN: 1118210824.

Blake, T. D. (1993). Hydrodynamics of wetting. In Berg, J. C., editor, *Wettability*, volume 6 of *Surfactant Science Series*, pages 251–309. CRC Press, Boca Raton, Florida, Vereinigte Staaten, ISBN: 0-8247-9046-4.

Blake, T. D. (2006). The physics of moving wetting lines. *Journal of Colloid and Interface Science*, 299(1):1–13, DOI: 10.1016/j.jcis.2006.03.051.

Blake, T. D. and De Coninck, J. (2002). The influence of solid–liquid interactions on dynamic wetting. *Advances in Colloid and Interface Science*, 96(1):21–36, DOI: 10.1016/S0001-8686(01)00073-2.

Blake, T. D. and Haynes, J. M. (1969). Kinetics of liquidliquid displacement. *Journal of Colloid and Interface Science*, 30(3):421–423, DOI: 10.1016/0021-9797(69)90411-1.

Bonn, D., Eggers, J., Indekeu, J., Meunier, J., and Rolley, E. (2009). Wetting and spreading. *Reviews of Modern Physics*, 81(2):739.

Burgmann, S., Barwari, B., and Janoske, U. (2018a). Inner flow structure of an adhering oscillating droplet in shear flow. In *19th International Symposium on Application of Laser and Imaging Techniques to Fluid Mechanics*, Lisbon.

Burgmann, S., Barwari, B., and Janoske, U. (2018b). Oscillation of adhering droplets in shear flow. In *5th International Conference on Experimental Fluid Mechanics*, Munich.

Cherry, B. W. and Holmes, C. M. (1969). Kinetics of wetting of surfaces by polymers. *Journal of Colloid and Interface Science*, 29(1):174–176, DOI: 10.1016/0021-9797(69)90367-1.

Chini, S. F. and Amirfazli, A. (2011). A method for measuring contact angle of asymmetric and symmetric drops. *Colloids and Surfaces A: Physicochemical and Engineering Aspects*, 388(1):29–37.

Chini, S. F., Bertola, V., and Amirfazli, A. (2013). A methodology to determine the adhesion force of arbitrarily shaped drops with convex contact lines. *Colloids and Surfaces A: Physicochemical and Engineering Aspects*, 436:425–433.

Couvreur, S. and Daerr, A. (2012). The role of wetting heterogeneities in the meandering instability of a partial wetting rivulet. *EPL (Europhysics Letters)*, 99(2):24004.

Cristini, V. and Tan, Y.-C. (2004). Theory and numerical simulation of droplet dynamics in complex flows - a review. *Lab on a Chip*, 4(4):257–264, DOI: 10.1039/B403226H.

Culkin, J. B. and Davis, S. H. (1984). Meandering of water rivulets. *AIChE Journal*, 30(2):263–267, DOI: 10.1002/aic.690300214.

Destatis (2017). Verkehr - Verkehrsunfälle. Report on statistical data Report number: 2080700177004, German Federal Statistical Office (Destatis).

Dianat, M., Skarysz, M., and Garmory, A. (2017a). A coupled level set and volume of fluid method for automotive exterior water management applications. *International Journal of Multiphase Flow*, 91:19–38, DOI: 10.1016/j.ijmultiphaseflow.2017.01.008.

Dianat, M., Skarysz, M., Hodgson, G., Garmory, A., and Passmore, M. (2017b). Coupled level-set volume of fluid simulations of water flowing over a simplified drainage channel with and without air coflow. *SAE Int. J. Passeng. Cars - Mech. Syst.*, 10(1):369–377, DOI: 10.4271/2017-01-1552.

Dimitrakopoulos, P. and Higdon, J. J. L. (1997). Displacement of fluid droplets from solid surfaces in low-Reynolds-number shear flows. *Journal of Fluid Mechanics*, 336:351–378, DOI: 10.1017/S0022112096004788.

DIN EN ISO 5801 (2011). Industrieventilatoren – leistungsmessung auf genormten prüfständen. International standard (german version).

Duffy, B. R. and Moffatt, H. K. (1995). Flow of a viscous trickle on a slowly varying incline. *The Chemical Engineering Journal and the Biochemical Engineering Journal*, 60(1):141–146, DOI: 10.1016/0923-0467(95)03030-1.

Durbin, P. A. (1988a). Considerations on the moving contact-line singularity, with application to frictional drag on a slender drop. *Journal of Fluid Mechanics*, 197:157–169, DOI: 10.1017/S0022112088003210.

Durbin, P. A. (1988b). On the wind force needed to dislodge a drop adhered to a surface. *Journal of Fluid Mechanics*, 196:205–222, DOI: 10.1017/S0022112088002678.

Dussan V., E. B. and Chow, R. T.-P. (1983). On the ability of drops or bubbles to stick to non-horizontal surfaces of solids. *Journal of Fluid Mechanics*, 137:1–29, DOI: 10.1017/S002211208300227X.

European legal directive Nr. 661/2009 (2009). Regulation concerning type-approval requirements for the general safety of motor vehicles, their trailers and systems, components and separate technical units intended therefore. European legal directive Nr. 661/2009, Parliament and Council of the European Union, https://eur-lex.europa.eu/eli/reg/2009/661/oj.

Fan, J., Wilson, M. C. T., and Kapur, N. (2011). Displacement of liquid droplets on a surface by a shearing air flow. *Journal of Colloid and Interface Science*, 356(1):286–292.

Fathi, N., Mertens, K., Putkaradze, V., and Vorobieff, P. (2014). Comment on "The role of wetting heterogeneities in the meandering instability of a partial wetting rivulet" by Couvreur S. and Daerr A. *EPL (Europhysics Letters)*, 108(5):54002, DOI: 10.1209/0295-5075/108/54002.

Fu, S. C., Leung, W. T., and Chao, C. Y. H. (2014). Detachment of droplets in a fully developed turbulent channel flow. *Aerosol Science and Technology*, 48(9):916–923, DOI: 10.1080/02786826.2014.938801.

Furmidge, C. G. L. (1962). Studies at phase interfaces. I. The sliding of liquid drops on solid surfaces and a theory for spray retention. *Journal of Colloid Science*, 17(4):309–324, DOI: 10.1016/0095-8522(62)90011-9.

Ganser, G. H. (1993). A rational approach to drag prediction of spherical and nonspherical particles. *Powder Technology*, 77(2):143–152, DOI: 10.1016/0032-5910(93)80051-B.

Gao, N., Geyer, F., Pilat, D. W., Wooh, S., Vollmer, D., Butt, H.-J., and Berger, R. (2017). How drops start sliding over solid surfaces. *Nature Physics*, 14:191–196, DOI: 10.1038/nphys4305.

Gloerfeld, M. (2017). *Experimental investigation of drops in shear flow*. Master's thesis, Technische Universität Darmstadt, Darmstadt, Germany.

Hagemeier, T., Hartmann, M., and Thévenin, D. (2011). Practice of vehicle soiling investigations: a review. *International Journal of Multiphase Flow*, 37(8):860–875, DOI: 10.1016/j.ijmultiphaseflow.2011.05.002.

Hecht, E. (2002). *Optics*. Addison-Wesley, San Francisco, USA, 4. ed., internat. ed. edition, ISBN: 0321188780.

Herrada, M. A., Mohamed, A. S., Montanero, J. M., and Gañán-Calvo, A. M. (2015). Stability of a rivulet flowing in a microchannel. *International Journal of Multiphase Flow*, 69:1–7, DOI: 10.1016/j.ijmultiphaseflow.2014.10.012.

Hoffmann, A. (2010). *Untersuchung mehrphasiger Filmströmungen unter Verwendung einer Volume-of-Fluid-ähnlichen Methode*. PhD thesis, Technische Universität Berlin, DOI: 10.14279/depositonce-2432.

Kistler, S. (1993). Hydrodynamics of wetting. In Berg, J. C., editor, *Wettability*, volume 49 of *Surfactant Science Series*, pages 311–430. CRC Press, Boca Raton, Florida, Vereinigte Staaten, ISBN: 0-8247-9046-4.

Lauga, E., Brenner, M. P., and Stone, H. A. (2007). Microfluidics: The no-slip boundary condition. In Tropea, C., Yarin, A. L., and Foss, J. F., editors, *Handbook of experimental fluid dynamics*, pages 1219–1240. Springer, Heidelberg, Germany, ISBN: 978-3-662-49162-1.

Le Grand-Piteira, N., Daerr, A., and Limat, L. (2006). Meandering rivulets on a plane: A simple balance between inertia and capillarity. *Physical Review Letters*, 96(25):254503, DOI: 10.1103/PhysRevLett.96.254503.

Lu, G., Wang, X.-D., and Duan, Y.-Y. (2016). A critical review of dynamic wetting by complex fluids: from Newtonian fluids to non-Newtonian fluids and nanofluids. *Advances in Colloid and Interface Science*, 236:43–62.

Madani, S. and Amirfazli, A. (2014). Oil drop shedding from solid substrates by a shearing liquid. *Colloids and Surfaces A: Physicochemical and Engineering Aspects*, 441:796–806.

Mahé, M., Vignes-Adler, M., Rousseau, A., Jacquin, C. G., and Adler, P. M. (1988). Adhesion of droplets on a solid wall and detachment by a shear flow: I. pure systems. *Journal of Colloid and Interface Science*, 126(1):314–328, DOI: 10.1016/0021-9797(88)90125-7.

Maleki, M., Reyssat, E., Quéré, D., and Golestanian, R. (2007). On the Landau-Levich transition. *Langmuir*, 23(20):10116–10122, DOI: 10.1021/la700822y.

Marmur, A. (2004). The lotus effect: Superhydrophobicity and metastability. *Langmuir*, 20(9):3517–3519, DOI: 10.1021/la036369u, 10.1021/la036369u. PMID: 15875376.

Marshall, J. S. and Ettema, R. (2004). Rivulet dynamics with variable gravity and wind shear. Technical report, submitted to the NASA Office of Biological and Physical Research, IIHR—Hydroscience & Engineering, College of Engineering, The University of Iowa, Iowa City, IA.

Mayrhofer, A. (2018). *Experimental investigation of shear driven drop interaction with grooves*. Bachelor's thesis, Technische Universität Darmstadt, Darmstadt, Germany.

Mertens, K., Putkaradze, V., and Vorobieff, P. (2005). Morphology of a stream flowing down an inclined plane. Part 1. Braiding. *Journal of Fluid Mechanics*, 531:49–58, DOI: 10.1017/S0022112005003873.

Milne, A. J. B. and Amirfazli, A. (2009). Drop shedding by shear flow for hydrophilic to superhydrophobic surfaces. *Langmuir*, 25(24):14155–14164.

Moghtadernejad, S. (2014). *Dynamics of Droplet Shedding and Coalescence under the Effect of Shear Flow*. Phd, Concordia University.

Moser, R. D., Kim, J., and Mansour, N. N. (1999). Direct numerical simulation of turbulent channel flow up to $Re_\tau = 590$. *Physics of Fluids*, 11(4):943–945.

Nakagawa, T. and Scott, J. C. (1984). Stream meanders on a smooth hydrophobic surface. *Journal of Fluid Mechanics*, 149:89–99, DOI: 10.1017/S002211208400255X.

Neinhuis, C. and Barthlott, W. (1997). Characterization and distribution of water-repellent, self-cleaning plant surfaces. *Annals of botany*, 79(6):667–677.

Oron, A., Davis, S. H., and Bankoff, S. G. (1997). Long-scale evolution of thin liquid films. *Reviews of Modern Physics*, 69(3):931.

Paulsen, R. (2017). *Das Stoppelfeldrennen*. Pixi-Serie 247. Carlsen, Hamburg, Germany, ISBN: 978-3-551-04306-1.

Pierce, E., Carmona, F. J., and Amirfazli, A. (2008). Understanding of sliding and contact angle results in tilted plate experiments. *Colloids and Surfaces A: Physicochemical and Engineering Aspects*, 323(1-3):73–82, DOI: 10.1016/j.colsurfa.2007.09.032.

Pilat, D. W., Papadopoulos, P., Schäffel, D., Vollmer, D., Berger, R., and Butt, H.-J. (2012). Dynamic measurement of the force required to move a liquid drop on a solid surface. *Langmuir*, 28(49):16812–20, DOI: 10.1021/la3041067.

Rettenmaier, D. (2019). *Numerical Simulation of Shear Driven Wetting*. PhD thesis, Technical University Darmstadt.

Reynolds, O. (1883). An experimental investigation of the circumstances which determine whether the motion of water shall be direct or sinuous, and of the law of resistance in parallel channels. *Philosophical Transactions of the Royal Society of London*, 174:935–982.

Roisman, I. V., Criscione, A., Tropea, C., Mandal, D. K., and Amirfazli, A. (2015). Dislodging a sessile drop by a high-Reynolds-number shear flow at subfreezing temperatures. *Phys Rev E*, 92(2):023007–5, DOI: 10.1103/PhysRevE.92.023007.

Ruckenstein, E. and Dunn, C. S. (1977). Slip velocity during wetting of solids. *Journal of Colloid and Interface Science*, 59(1):135–138, DOI: 10.1016/0021-9797(77)90347-2.

Schleizer, A. D. and Bonnecaze, R. T. (1999). Displacement of a two-dimensional immiscible droplet adhering to a wall in shear and pressure-driven flows. *Journal of Fluid Mechanics*, 383:29–54, DOI: 10.1017/S0022112098003462.

Schlichting, H. and Gersten, K. (2006). *Grenzschicht-Theorie*. Springer, Heidelberg, Germany, ISBN: 9783540230045.

Schmuki, P. and Laso, M. (1990). On the stability of rivulet flow. *Journal of Fluid Mechanics*, 215:125–143, DOI: 10.1017/S0022112090002580.

Sedev, R. V. and Petrov, J. G. (1991). The critical condition for transition from steady wetting to film entrainment. *Colloids and Surfaces*, 53(1):147–156, DOI: 10.1016/0166-6622(91)80041-L.

Seiler, P. M., Gloerfeld, M., Roisman, I. V., and Tropea, C. (2019). Aerodynamically driven motion of a wall-bounded drop on a smooth solid substrate. *Phys. Rev. Fluids*, 4:024001, DOI: 10.1103/PhysRevFluids.4.024001.

Shikhmurzaev, Y. D. (1993). The moving contact line on a smooth solid surface. *International Journal of Multiphase Flow*, 19(4):589–610, DOI: 10.1016/0301-9322(93)90090-H.

Shing Chan, T., Gueudré, T., and Snoeijer, J. H. (2011). Maximum speed of dewetting on a fiber. *Physics of Fluids*, 23(11):112103, DOI: 10.1063/1.3659018.

Snoeijer, J. H., Andreotti, B., Delon, G., and Fermigier, M. (2007). Relaxation of a dewetting contact line. Part 1. A full-scale hydrodynamic calculation. *Journal of Fluid Mechanics*, 579:63–83, DOI: 10.1017/S0022112007005216.

Stout, K. J. and Blunt, L. (2001). A contribution to the debate on surface classifications—random, systematic, unstructured, structured and engineered. *International Journal of Machine Tools and Manufacture*, 41(13):2039–2044, DOI: 10.1016/S0890-6955(01)00069-4.

Tarquini, S., Antonini, C., Amirfazli, A., Marengo, M., and Palacios, J. (2014). Investigation of ice shedding properties of superhydrophobic coatings on helicopter blades. *Cold Regions Science and Technology*, 100:50–58.

Theodorsen, T. and Clay, W. C. (1933). Ice prevention on aircraft by means of engine exhaust heat and a technical study of heat transmission from a Clark Y airfoil. Technical Report 403, National Advisory Committee for Aeronautics. Langley Aeronautical Lab.; Langley Field, VA, United States. Document ID 19930091477.

Towell, G. D. and Rothfeld, L. B. (1966). Hydrodynamics of rivulet flow. *American Institute of Chemical Engineers Journal*, 12(5):972–980, DOI: 10.1002/aic.690120524.

Tropea, C., Yarin, A. L., and Foss, J. F. (2007). *Springer Handbook of Experimental Fluid Dynamics*. Springer, Heidelberg, Germany, ISBN: 978-3-662-49162-1.

Trujillo-Pino, A., Krissian, K., Alemán-Flores, M., and Santana-Cedrés, D. (2013). Accurate subpixel edge location based on partial area effect. *Image and Vision Computing*, 31(1):72–90, DOI: 10.1016/j.imavis.2012.10.005.

Voinov, O. V. (1976). Hydrodynamics of wetting. *Fluid Dynamics*, 11(5):714–721, DOI: 10.1007/bf01012963.

Wickersheim, R. (2019). *Experimental investigation of rivulet behavior on smooth rigid substrates*. Bachelor's thesis, Technische Universität Darmstadt, Darmstadt, Germany.

Wolansky, G. and Marmur, A. (1999). Apparent contact angles on rough surfaces: The Wenzel equation revisited. *Colloids and Surfaces A: Physicochemical and Engineering Aspects*, 156(1):381–388.

Young, T. et al. (1805). Iii. an essay on the cohesion of fluids. *Philosophical transactions of the royal society of London*, 95:65–87.

A Long-term environmental influence on surfaces

The importance of the surface wettability, specifically the contact angles, became apparent throughout the last chapters. This importance in reference vehicle exterior water management, resulted in a long term study. As summarized in the introduction, exterior water management is currently investigated in environmental wind tunnels. Before each of these experiments the vehicles are thoroughly cleaned. Cleaning returns the car to a uniform state, which does not consider the long-term influence of exposure to the environment.

Few investigations exist on how surface wettability changes over time, when a car is exposed to varying weather conditions. For this reason a study on the long-term changes has been performed and is presented in this chapter.

A.1 Vehicle and experimental procedure

A car used for short-term commuting, that regularly is parked outside, has been used for these investigations. An image of the vehicle is shown in Figure A.1. Before the initial measurement the vehicle was thoroughly cleaned and a coating of wax was applied in an automated car wash.

Six measurement positions on the surface were chosen. The selected locations needed to fulfill two essential criteria. First, the markers specifying the location had to be outside of any viewing area. Second, different substrates should be investigated. The six locations are marked using roman numerals in Figure A.1. The hood of the car made from varnished plastic (I) was selected as the first location. Three measurements on glass surfaces were made: windscreen (II), rear side window top (III) and bottom (IV). One

measurement on varnished steel (V) on the rear of the vehicle and lastly on the acrylic glass of the headlight.

Figure A.1: Photograph of the car used for the long-term study. Measurement locations are indicated by roman numerals.

Since measuring advancing and receding contact angles currently is not feasible outside of a laboratory environment, a mobile device able to measure equilibrium contact angles, has been used. This device, Mobile Surface Analyzer (MSA) by Krüss GmbH, is a hand-held measurement device. It consists of three components: a pressure driven dosing mechanism, a light source and a low speed camera. The dosing mechanism is capable of placing two independent drops with different liquids on the substrate. Both liquids are stored in specialized tubes that are pressurized. The tubes are connected to two magnetic valves that can open for a set time. The combination of pressure in the tube and duration of the valve being open allows depositing drops with a specific volume onto a surface. The background lighting and camera are adjusted in a way that a sharp shadowgraphy image of the drops can be recorded. The device is connected via USB3 to a laptop on which the images are stored and directly analyzed. The software controlling the hand held device offers various algorithms for the image analysis.

One set of measurements results in one value for each location. At each location the same three positions less than 10 mm apart from each other are chosen. At each of the three locations the same procedure is performed. An initial 1 μl drop is placed and its volume is increased to 5 μl in four steps. For each placed volume a shadowgraphy image is taken. In total this results to 15 contact angle measurements for each of the six location on the vehicle. These 15 measurements are averaged to one value.

Fourteen sets of measurements were made over 238 days with around 17 days between each measurement. The first measurement was recorded directly after the car was cleaned on Tuesday 19$^{\text{th}}$ September 2017. The last measurement was recorded shortly before the vehicle needed to be cleaned for necessary repairs on Tuesday 15$^{\text{th}}$ of May 2018.

A.2 Contact angle evolution over time

The evolution of the equilibrium contact angle for each of the six measurement points is shown in Figure A.2. The equilibrium contact angle on the ordinate is plotted over the day of the experiment. Day 0 is the day when the car was cleaned. At each position a contact angle between 65° and 75° was recorded. This is not surprising, considering a coating of car wax was added to all surfaces. The effect of the coating is present up to the third set of measurements on the 37$^{\text{nd}}$ day, where the contact angles on the side windows decrease by 10° to 15° degrees.

A trend that the equilibrium contact angle decreases over time is clearly visible. After 240 days, angles between 25° and 40° have been measured on the glass surfaces, values half the size of the initially measured ones. On the varnished substrates a decrease by 15°. From the measured data it is not possible to determine if further changes of the contact angles are to be expected, although the trend indicates that this is quite probable.

At day 181 a strong change in contact angle occurs on the windscreen and the headlight. On the windscreen contact angles of 30°, about half the previous value were measured. A reduction by about 15° was observed on the headlight. At day 199 for both surfaces values around 55° were measured again. This change in contact angles may be connected to snow fall

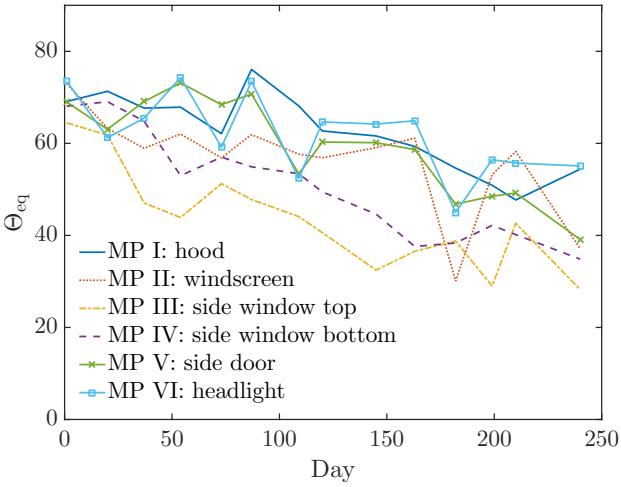

Figure A.2: Θ_{eq}-Day diagram for all measurement positions.

on March 18th 2018 (day 180) of the experiment which was followed by rain on March 22nd 2018.

As stated in Section 1.1, the side windows are of great importance for exterior water management, since no active system ensures a clear line of sight. Due to this importance and the fact that on the side window the most prominent changes in contact angle have been observed, the corresponding measurements are shown in Figure A.3. The dashed red and solid blue line in the diagram represent the mean equilibrium contact angles on the top and bottom of the side window. The bars show the lowest and highest value recorded during the 15 individual measurements at that point.

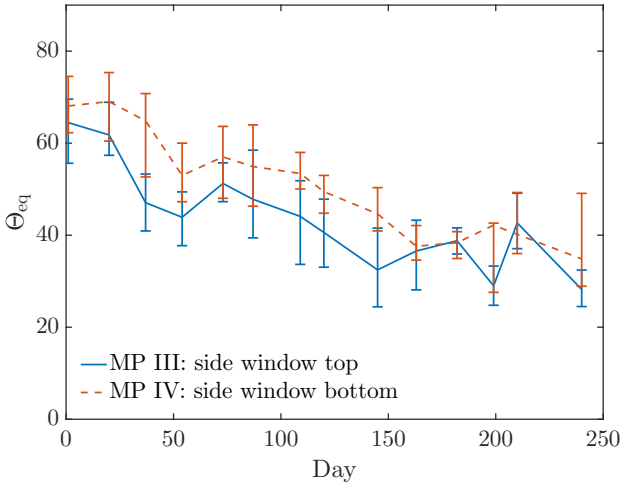

Figure A.3: Θ_{eq}-Day diagram for the side window measurements. Bars represent the minimal and maximal value recorded during each set of measurements.